Joule

CellPress
OPEN ACCESS

Article

# Tailoring perovskite crystallization and interfacial passivation in efficient, fully textured perovskite silicon tandem solar cells

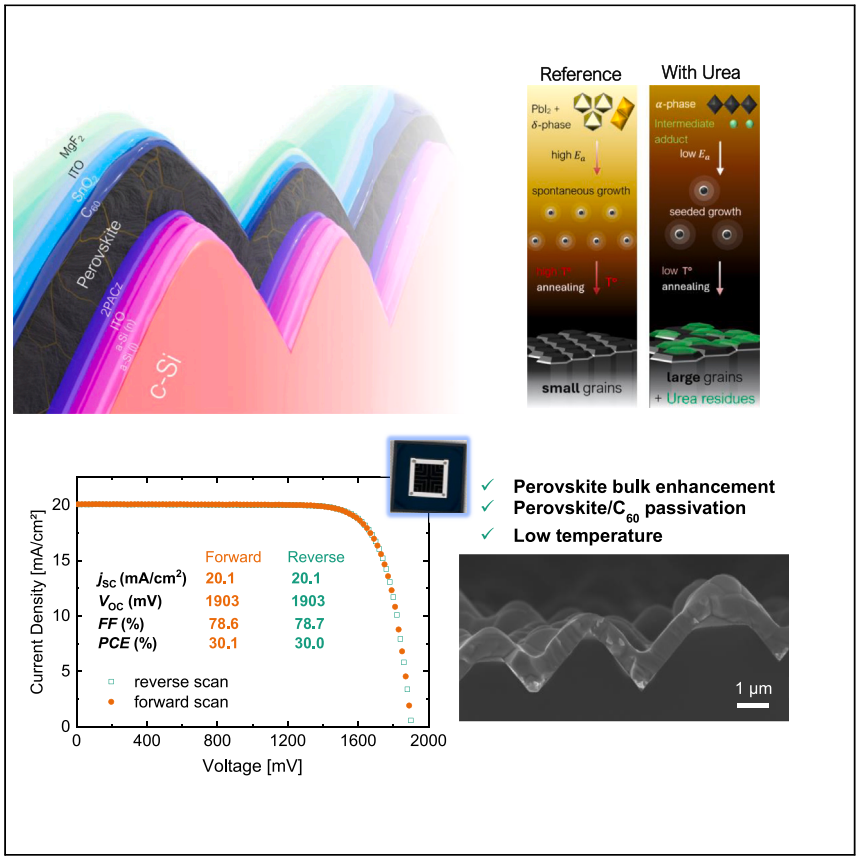


Perovskite silicon tandem solar cells must demonstrate high efficiency and low manufacturing costs to be considered as a contender for wide-scale photovoltaic deployment. In this work, we propose the use of a single additive that enhances the perovskite bulk quality and passivates the perovskite/C60 interface, thus tackling both main issues in industry-compatible fully textured perovskite silicon tandems. Besides enhancing the efficiency to 30%, this approach enables the reduction of manufacturing steps, which is desirable to reduce production costs.

Oussama Er-raji, Mohamed A.A. Mahmoud, Oliver Fischer, ..., Juliane Borchert, Stefan W. Glunz, Patricia S.C. Schulze

oussama.er-raji@ise.fraunhofer.de

## Highlights

Perovskite silicon tandems with 30% efficiency using industry-compatible silicon wafers

Single perovskite additive enhances both perovskite bulk and perovskite/$C_{60}$ interface

Additive (urea) approach implemented at a low perovskite annealing temperature of 100°C

Better understanding of perovskite formation on large silicon pyramids

Er-raji et al., Joule 8, 2811–2833
October 16, 2024 
Published by Elsevier Inc.
https://doi.org/10.1016/j.joule.2024.06.018

Joule

CellPress
OPEN ACCESS

Article

# Tailoring perovskite crystallization and interfacial passivation in efficient, fully textured perovskite silicon tandem solar cells

Oussama Er-raji,[1,2,7,*] Mohamed A.A. Mahmoud,[1,2] Oliver Fischer,[1,2] Alexandra J. Ramadan,[3] Dmitry Bogachuk,[1,6] Alexander Reinholdt,[4] Angelika Schmitt,[4] Bhushan P. Kore,[1,2] Thomas William Gries,[5] Artem Musiienko,[5] Oliver Schultz-Wittmann,[1] Martin Bivour,[1] Martin Hermle,[1] Martin C. Schubert,[1] Juliane Borchert,[1,2] Stefan W. Glunz,[1,2] and Patricia S.C. Schulze[1]

## SUMMARY

**Fully textured perovskite silicon tandem solar cells are promising for future low-cost photovoltaic deployment. However, the fill factor and open-circuit voltage of these devices are currently limited by the high density of defects at grain boundaries and at interfaces with charge transport layers. To address this, we devise a strategy to simultaneously enhance perovskite crystallization and passivate the perovskite/$C_{60}$ interface. By incorporating urea ($CO(NH_2)_2$) as an additive in the solution step of the hybrid evaporation/spin-coating perovskite deposition method, the crystallization kinetics are accelerated, leading to the formation of the desired photoactive phase at room temperature. With that, perovskite films with large grain sizes (>1 μm) and improved optoelectronic quality are formed at low annealing temperatures (100°C). Concurrently, remnant urea molecules are expelled at the perovskite surface, which locally displaces the $C_{60}$ layer, thus reducing interfacial non-radiative recombination losses. With this strategy, the resulting tandem solar cells achieve 30.0% power conversion efficiency.**

## INTRODUCTION

Building on existing silicon production technology, fully textured perovskite silicon tandem solar cells (FT-TSCs) promise to be a low-cost and high-efficiency future technology for large-scale photovoltaic deployment.[1–5] The use of textured silicon with >2 μm pyramid height makes the tandem solar cell compatible with industry standards. Furthermore, the conformal perovskite top-cell deposition enables efficient light in-coupling owing to the double-bounce effect,[6] which is not possible in state-of-the-art designs (S-TSCs), namely with flat-front or textured-front silicon-bottom solar cells with small pyramid size (<2 μm) where the perovskite top cell submerges the small pyramids.[7–9] Yet, despite the intrinsic optical advantage, which is reflected in a high short-circuit current density ($j_{SC}$) generation, reaching a high power conversion efficiency (*PCE*) is only possible if the open-circuit voltage ($V_{OC}$) and fill factor (*FF*) of the device are preserved at a high level.[10]

Therefore, the current published *PCE* records are held by S-TSCs with either flat-front bottom cell,[11] or textured-front with small pyramid size (<2 μm),[12] where spin-coating was used as the processing method. However, as spin-coating is not compatible with micrometer-sized pyramids for FT-TSCs,[13] an alternative approach can be used—the

## CONTEXT & SCALE

Fully textured perovskite silicon tandem solar cells rely on the deposition of the perovskite absorber on textured silicon with a >1 μm pyramid size, which represents the current standard in the industry. To bridge the gap between research and industry, these cells must demonstrate a high power output. Nevertheless, perovskite absorbers deposited on large pyramids often suffer from a high grain boundary defect density and poor interfacial passivation at the perovskite/electron transport layer ($C_{60}$) junction. We tackle both loss mechanisms by introducing a multi-functional additive (urea), which simultaneously regulates the perovskite crystallization as well as passivates the perovskite/$C_{60}$ interface. Moreover, this strategy is employed at a low annealing temperature (100°C, different from the standardly used 150°C), thus enabling an effective lowering of the perovskite annealing's thermal budget. This approach is of high relevance for the industrialization of perovskite silicon tandem solar cells.

so-called hybrid method.[14–24] It consists of two steps: (1) thermal evaporation of inorganic perovskite compounds, which form a uniform scaffold on textured silicon, and (2) organohalide wet-chemical deposition step, where organic perovskite compounds are infiltrated to react with the pre-deposited scaffold. Following annealing of the substrate, perovskite crystallization takes place, forming a photoactive layer.

Despite significant developments in the *PCE*,[23] limited attention is given to the crystallization dynamics of the hybrid method. Perovskite films deposited by the hybrid approach usually have inferior grain size, crystal quality, and optoelectronic properties in comparison to their spin-coated counterparts.[25] Additionally, the high defect density generated at the contact between the perovskite surface and the commonly used electron transport layer (ETL) $C_{60}$ further exacerbates the radiative efficiency of the device.[26–29] Several attempts on circumventing the non-radiative recombination losses were shown, which focused on providing individual solutions for perovskite crystallization and perovskite surface passivation.[16,18,23] Recently, Chin et al. employed pentafluorobenzyl phosphonic acid as a perovskite additive that successfully enhanced the perovskite morphology by retarding the crystallization kinetics and passivated the perovskite/$C_{60}$ interface. The employed perovskite annealing temperature, similar to previous works with the hybrid method (150°C; see Table S1 in supplemental information), is regarded as unfavorable since it has been observed to degrade some underlying organic hole transport layers (HTLs),[14,30] which are desirable since they allow conformal coating of the pyramids. To comply with the high annealing temperature strategy, to date, literature reports either employ spin-coated self-assembling monolayers (SAMs) or alternatively replace the ITO interconnection layer by a nanocrystalline silicon tunnel junction, which enables better sticking of evaporated HTLs.[17,19,31]

Considering the industrial manufacturing perspective of the FT-TSC technology, low-temperature processes and minimum fabrication steps are desired. Therefore, there exists a need for a quick and efficient method that tackles the following 3 aspects: (1) enhancing the perovskite bulk quality, (2) reducing the interfacial losses at the perovskite/$C_{60}$ interface, and (3) reducing the perovskite annealing temperature to enable flexibility of choice of underlying charge transport layers (CTLs). Here, we introduce $CO(NH_2)_2$ (urea), a cheap, mass-produced, and non-hazardous compound that fulfills all three requirements. By exploiting the strong interaction of urea with solution precursors, the crystallization kinetics are accelerated, and the perovskite $\alpha$-phase is obtained during the organohalide/evaporated scaffold intermixing step at room temperature. This enables a seeding growth crystallization mechanism where perovskite films with large grain size (>1 μm) and improved structural and opto-electronic quality can be obtained with annealing temperatures as low as 100°C. Additionally, by controlling the crystallization sequence, remnant urea molecules reside at the perovskite surface, thus displacing the $C_{60}$ contact, which reduces the severe interfacial non-radiative recombination losses. With these benefits, an average increase of 2.4%$_{abs.}$ in *PCE* was obtained for urea-treated FT-TSCs in comparison to reference devices. By further optimizing the functional layers, the champion device delivered a 30.0% stabilized *PCE*. This work provides an effective method to boost the performance of FT-TSCs, thereby continuing the efforts of bringing this technology closer to commercialization.

## RESULTS AND DISCUSSION

The simultaneous low-temperature crystallization and surface passivation strategy developed in this work is based on the incorporation of urea as an additive during

[1]Fraunhofer Institute for Solar Energy Systems ISE, Heidenhofstr. 2, 79110 Freiburg, Germany

[2]Chair of Photovoltaic Energy Conversion, Department of Sustainable Systems Engineering (INATECH), University of Freiburg, Emmy-Noether-Str.2, 79110 Freiburg, Germany

[3]Department of Physics and Astronomy, University of Sheffield, Hicks Building, Hounsfield Road, Sheffield S3 7RH, UK

[4]Fraunhofer Institute for Silicate Research ISC, Neunerpl. 2, 97082 Würzburg, Germany

[5]Helmholtz-Zentrum Berlin für Materialien und Energie GmbH, Kekulestraße 5, 12489 Berlin, Germany

[6]Present address: Solarlab Aiko Europe GmbH, Berliner Allee 29, 79110 Freiburg, Germany

[7]Lead contact

*Correspondence: oussama.er-raji@ise.fraunhofer.de

https://doi.org/10.1016/j.joule.2024.06.018

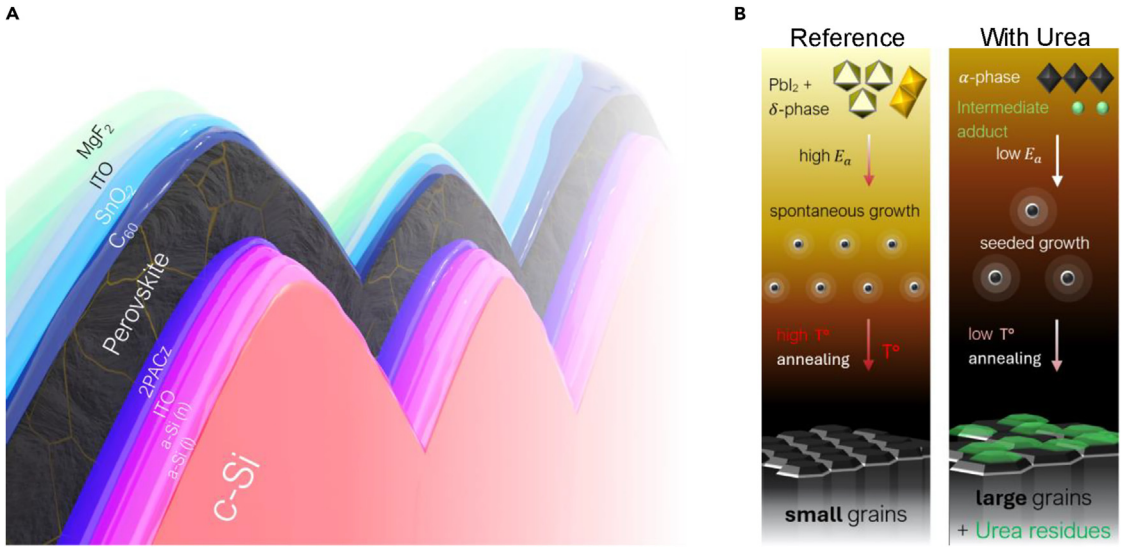


**Figure 1. Schematic depicting**

(A) The fully textured perovskite silicon tandem solar cell architecture and (B) the impact of urea on accelerating the crystallization kinetics and final perovskite film quality.

perovskite film fabrication. It is a strong Lewis base additive that has been previously demonstrated to enhance the quality of solution-processed perovskites via formation of intermediate adducts between urea and $PbI_2$ in the precursor solution.[32–36] Furthermore, it is a non-hazardous, cheap, and mass-produced compound, which fits in the picture of the use of the hybrid route fabrication technique, which uses green solvents such as ethanol (EtOH) or isopropanol.

The hybrid evaporation/spin-coating route is employed to conformally form perovskite films on industrially relevant, micrometer-sized random pyramid texture (Figure 1A). In a first step, CsI and $PbI_2$ are co-evaporated to form a 550 nm thick inorganic scaffold (Figure S1). Then, an organic salt solution containing FABr and FAI (FA: formamidinium) in EtOH is spin-coated dynamically on the pre-deposited scaffold. Finally, an annealing step is conducted in air at 150°C for 25 min to induce perovskite crystallization. For urea-treated perovskite films, 5 mg/mL of urea is added in the organohalide solution mixture to alter the crystallization kinetics (Figure 1B). Furthermore, the annealing step is reduced to 100°C for 10 min. More details are provided in the experimental section.

## Perovskite film morphological, structural, and optoelectronic properties

We first assess the impact of urea on the morphological and structural properties of the perovskite absorber using samples consisting of textured silicon/ITO/2PACz/perovskite (Figure 2A), which are also used in our FT-TSCs. Figures 2B and 2C show top-view and cross-sectional scanning electron microscopy (SEM) images of reference and urea-treated perovskite films. Both absorbers show uniform layer formation on textured silicon with no voids/pinholes and with a comparable thickness approaching 630 $\pm$ 25 nm. With the addition of urea, the average apparent grain size is substantially increased from ~200 nm (reference) up to >1 μm as highlighted in top-view SEM images and confirmed in atomic force microscopy (AFM) images (Figure S2). Furthermore, cross-sectional SEM imaging reveals that the urea-treated absorber exhibits a columnar character of the grains enabling single-grain perovskite structures along the perpendicular direction to the substrate

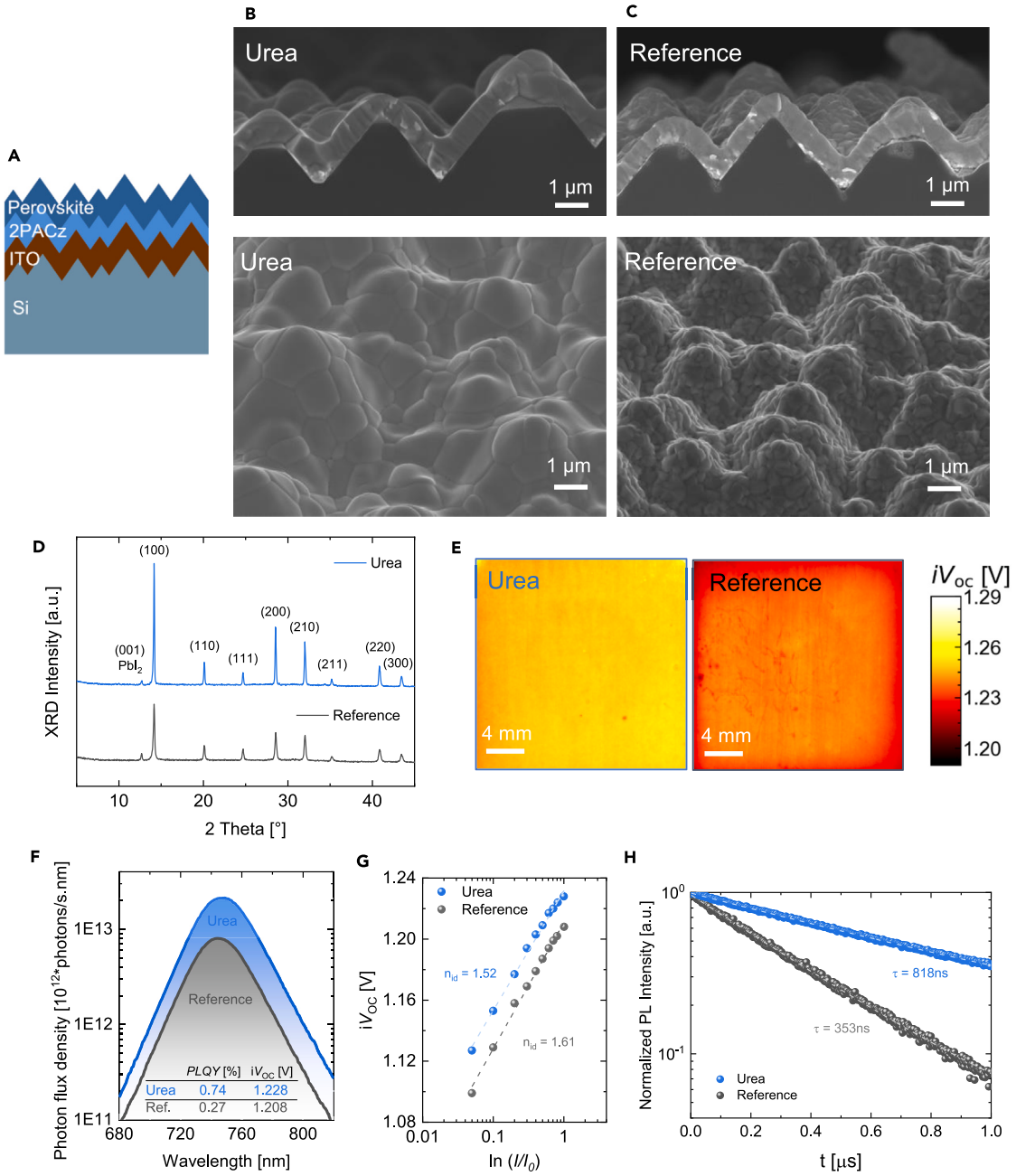


**Figure 2. Morphological, structural, and optoelectronic characterization of perovskite films on textured silicon**

(A) Schematic structure of the probed textured silicon/ITO/2PACz/perovskite half-stacks. Textured silicon/ITO/2PACz/perovskite half-stacks with urea (in blue) and without urea (in gray, reference) characterized via (B and C) cross-sectional and top-view scanning electron microscopy (SEM), (D) X-ray diffraction, (E) photoluminescence (PL)-based implied open-circuit voltage ($iV_{OC}$) imaging, (F) spectrally resolved steady-state *PLQY*, (G) intensity-dependent steady-state *PLQY*, and (H) transient PL.

(Figure 2B). By contrast, a high density of grain boundaries is observed in the reference film (Figure 2C).

We further investigated the crystalline quality of perovskite absorbers using X-ray diffraction (XRD). Notably, the intensity of the main perovskite peak (100) of films with urea is significantly enhanced in comparison to the reference. As Figures 2B

and 2C do not show an obvious thickness change, we ascribe the enhanced crystallinity of the urea-treated perovskite to the large grain size formation, in contrast to the multi-grain structure of the reference film. Moreover, the respective full-width-at-half-maximum (FWHM) is decreased from 0.21° to 0.12°, which indicates an enlarged crystal size. Besides the perovskite phase, $PbI_2$ was detected in both perovskite films with the characteristic (001) peak at 12.69°.[37] For the hybrid route, the $PbI_2$ detection typically stems from an incomplete conversion of $PbI_2$ precursor to perovskite. It is usually found at the bottom perovskite/HTL interface due to a gradient of the interdiffused organohalides during the wet-chemical step. Complementing the measured XRD patterns, cross-sectional SEM images of the reference films still contain unreacted $PbI_2$ grains (particularly visible in the pyramid valleys), which are recognized via bright appearance due to higher density of heavy atoms in Figure 2C. By contrast, urea-treated films show significantly lower residual $PbI_2$, which is expected to enhance the charge transfer at the perovskite/HTL interface.

Next, we performed spectrally resolved steady-state photoluminescence (PL) measurements to evaluate urea's impact on the perovskite's optoelectronic quality. Overall, a higher PL peak intensity was found in presence of urea, indicating an inhibition of non-radiative recombination in the polycrystalline bulk (Figure 2F). Furthermore, we noted a slight 0.01 eV red-shift of the PL peak position from the reference (1.67 eV) to the urea-treated absorber (1.66 eV). The extracted PL quantum yield (*PLQY*) of the urea-treated perovskite (0.74%) was triple that of the reference (0.25%), which translates to a 20 mV increase in the implied $V_{OC}$ ($iV_{OC}$) of the stack. Given the 1.374 and 1.365 V radiative limits of semiconductors with 1.67 and 1.66 eV bandgaps (approximated at the first degree with the generalized Planck law),[38] it can be concluded that the voltage deficit attributed to non-radiative recombination losses mainly in the bulk of the polycrystalline perovskite film is remarkably reduced in presence of urea (137 mV) in comparison to reference (166 mV). While Figure 2F shows $iV_{OC}$ values at an excitation fluence that is relevant for device operation (1 sun illumination), we performed in a second step intensity-dependent *PLQY* measurements and extracted the respective $iV_{OC}$ values (Figure 2G). For all probed fluences, we observed an enhancement in $iV_{OC}$ for the urea-treated perovskite absorber. Furthermore, an internal ideality factor ($n_{id}$) of 1.52 was found, which is lower than that of the reference perovskite (1.61). A smaller value of $n_{id}$ toward a value of 1 is typically associated with a predominant bimolecular radiative and reduced trap-assisted Shockley-Read Hall recombination, which hints toward higher $V_{OC}$ and *FF* potential with urea incorporation.[39] Besides assessing local changes via spectrally resolved PL, we evaluate the spatial distribution over the substrate using PL-based $iV_{OC}$ imaging.[40] Figure 2E confirms the 20 mV increase in $iV_{OC}$ in a homogeneous manner at 1-sun illumination intensity. Extending the optoelectronic study, we performed time-resolved PL (trPL) measurements to gain additional information about charge carrier dynamics (Figure 2H). The reduced non-radiative recombination in the urea-treated film was further evidenced with a long PL decay and effective charge carrier lifetime of 818 ns in contrast to 353 ns for the reference film (also confirmed at different laser intensities as depicted in Figure S3).

### Urea working mechanism for large grain growth at low annealing temperature

To gain insight into the perovskite crystallization mechanism in presence of urea, we performed XRD and steady-state PL measurements at different processing steps. Upon co-evaporation of the CsI/$PbI_2$ inorganic scaffold, the film presents a crystalline structure characterized by a dominant $PbI_2$ peak at 12.69° (Figure 3A). While not clearly visible in the plain diffractogram, a peak at 9.94° becomes more visible when plotting the diffractogram logarithmically, which denotes the $\delta$-$CsPbI_3$ phase

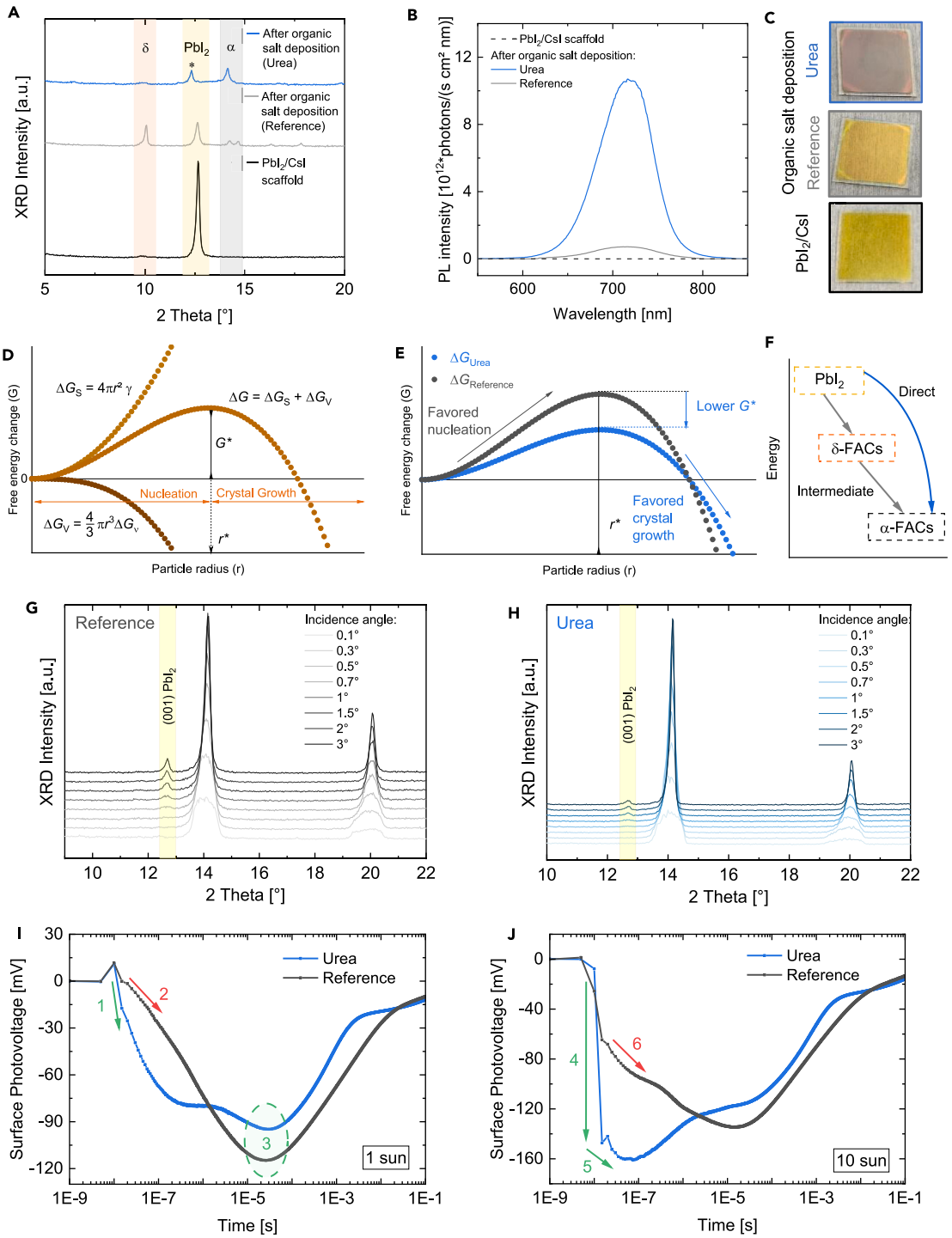


**Figure 3. Investigation of urea's working mechanism for large perovskite grain growth and reduced remnant $PbI_2$ through optical, structural, and optoelectronic characterization at different processing steps and its implications on the interfacial perovskite/hole transport layer quality**

(A and B) (A) X-ray diffraction (XRD) measurements and (B) steady-state photoluminescence measurements realized on the evaporated CsI/$PbI_2$ scaffold (in black), organic salt deposition without urea (reference, gray) and with urea (blue) on top of the scaffold directly after spin-coating. The measurements are realized on textured silicon/ITO/2PACz substrates.

(C) Optical images of samples with similar layer stack and color code as (B) but processed on glass substrates to visualize the films' color change.

(D) The Gibbs free energy as a function of particle radius and its components (surface and volume terms) adapted from Choi et al.[41]

**Figure 3. *Continued***

(E) Schematic representation of the evolution of the Gibbs free energy during the crystallization without and with urea incorporation based on the different characterizations during film fabrication.

(F) A schematic showing the difference in energy of the $PbI_2$ precursor phase and $\delta$- and $\alpha$-perovskite phases adapted from Zhang et al.[22]

(G and H) Grazing-incidence XRD diffractograms of perovskite films with/without urea on textured silicon/ITO/2PACz substrates for different incident beam angles.

(I and J) Transient surface photovoltage measurements of perovskite films with/without urea on textured silicon/$Al_2O_3$/ITO/2PACz substrates at 1-sun and 10-sun laser equivalent intensity, respectively.

(Figure S4A).[22] No PL response was recorded (Figure 3B), and the film appearance on optical glass was yellow (Figure 3C). Upon deposition of the FABr/FAI organohalide solution (reference), the $PbI_2$ peak intensity is reduced, and the $\delta$-perovskite peak intensity at 10° is significantly increased. To assess the composition of the prominent $\delta$-phase after solution infiltration, we deposited individual solutions of FAI, FABr, and FABr/FAI mix on the inorganic scaffold. As highlighted in Figure S4B, the peak position shifts according to the iodide to bromide ratio (ionic radii 220 and 196 pm, respectively),[42] moving from 9.91° with a pure FAI solution to 10.18° with a pure FABr solution. As a result, the $\delta$-perovskite composition is $\delta$-$FA_yCs_{1-y}Pb(I_xBr_{1-x})_3$. While two small-intensity peaks appear at 14.21° and 14.67°, the dominant perovskite phase is the $\delta$-$FA_yCs_{1-y}Pb(I_xBr_{1-x})_3$ phase, and the optical appearance of the film on a glass substrate is yellow (Figure 3C). With addition of urea to the organohalide solution, the crystallization pathway is altered. The diffraction peak of crystalline $PbI_2$ at 12.69° is eliminated, and a peak at 12.34° appears (ascribed to an intermediate adduct formed between all precursors of the system; see Figures S4C and S4D). The intermediate $\delta$-phase perovskite is not present, and the $\alpha$-phase perovskite is dominant at room temperature. These rapid changes in the intermediate phases imply that the reaction between organic and inorganic precursors is significantly accelerated in the presence of urea. As a result, the PL intensity of the urea-treated film directly after spin-coating is nearly 10 times higher than the reference sample with a remarkably narrow FWHM. Furthermore, the film morphology on textured silicon shows clearly defined perovskite grains, while no indication of such is reflected by the reference film morphology (Figure S5), and the optical appearance of the film on a glass substrate is brown. Videos S1 and S2 further document the optical transformation of the film during the spin-coating step of organohalides with/without urea.

The combination of optical, structural, and optoelectronic characterization results during perovskite film growth can be linked with the thermodynamic laws of crystallization to explain the enhanced perovskite formation pathway in the presence of urea. Classically, crystallization can be modeled by two steps: nucleation and crystal growth.[41,43–46] The nuclei formation process directly depends on the critical radius ($r^*$) of the nuclei as well as the critical Gibbs free energy $G^*$, which is set by the surface and volume parts of the Gibbs free energy (Figure 3D). That is, when the nuclei have radii smaller than $r^*$, they cannot overcome the critical free energy barrier and get redissolved; however, when the radii of the nuclei are greater than $r^*$, they are thermodynamically stable and can further grow to form crystals.[41,43–46] From the diagram in Figure 3D, it can be deduced that lowering the critical Gibbs free energy favors nuclei to overcome the energy barrier and grow into crystals. As pre-determined from the XRD results directly after spin-coating, the presence of urea in the solution lowers the critical Gibbs free energy for formation of the black $\alpha$-perovskite phase. This might be explained by a reduction of the surface energy component (Figure 3D) due to a competitive interaction of N and O from urea to coordinate with Pb from the scaffold, which drives a configurational transition of the $Pb(I_yBr_{1-y})_6$ octahedra from face-sharing to corner-sharing. It is a similar effect to that observed with other Lewis

base solvents (DMF, DMSO, and NMP) as well as other substances such as Cl-, SCN-, and alkylammonium chlorides reported to drive the formation of $\alpha$-$FAPbI_3$ at low temperatures.[47–52] As such, the crystallization model in presence of urea can be represented by a reduced critical Gibbs free energy as we illustrate in Figure 3E, thus enabling a faster transition to the growth phase. By contrast, nuclei are more prone to redissolution in the reference case before reaching the critical radius $r^*$, as evident from the appearance of the intermediate high-energy $\delta$-$FA_yCs_{1-y}Pb(I_xBr_{1-x})_3$ phase represented in Figure 3F. As a result, even prior to the annealing step, urea enables the formation of nucleation sites from which perovskite growth is initiated during the annealing step (since it is more thermodynamically favorable than the formation of new seeds), thus allowing for the growth of large crystalline domains, even at a low temperature (100°C).[53]

We further investigated the impact of higher annealing temperatures, e.g., 125°C, 150°C, and 175°C, but no change in apparent grain size or crystallinity was noted (Figure S6). Therefore, it can be concluded that the addition of urea effectively lowers the thermal budget of the annealing step while conserving a high perovskite quality. By contrast, in the absence of urea (reference), the nucleation process is predominantly taking place during the annealing step alongside the crystal growth process. This leads to the formation of perovskite films with low apparent grain size and reduced crystallinity (Figure 2). Moreover, Figure S7 shows that lowering down the annealing temperature from 150°C to 100°C without urea additive further reduces the perovskite's bulk and surface quality, thus rationalizing the use of high annealing temperatures in literature where the hybrid deposition method is adopted.

Next, using grazing-incidence XRD (GI-XRD), we investigate the impact of urea on remnant $PbI_2$. In contrast to standard Bragg-Brentano (BB) geometry, GI-XRD enables a more sensitive analysis of the structural composition of the perovskite absorber at different depths. By increasing the incidence angle $\theta$ from 0.1° to 3°, we scan the perovskite absorber from the top surface toward the bottom interface with the underlying HTL. While the presence of crystalline $PbI_2$ precursor material is manifested at 1° for the reference perovskite film, it only appears at an angle $\theta$ equivalent to 1.5° in the urea-treated film (Figures 3G and 3H). Thus, it can be concluded that urea contributes to the reduction of residual $PbI_2$.

Taking into account the Lewis base nature of urea, the lone electron pairs of the donor atom oxygen are likely to coordinate to the unoccupied orbital of $PbI_2$, leading to the formation of a stable Lewis acid-base intermediate adduct.[32,34,54] We hypothesize that the presence of such an adduct expands the layer spacing of the $PbI_2$ lattice. Indeed, recent literature reports have demonstrated that forming $PbI_2$ from a $PbI_2$/DMF solution doped with urea changes the film's morphology from compact to porous[34]; furthermore, other Lewis base additives such as DMSO have similarly been shown to pre-expand the lattice spacing of $PbI_2$.[55,56] As a result, the diffusion and intercalation of organohalides (FA*X*, *X* = Br, I) into the lattice structure of the crystalline $PbI_2$ layer are facilitated. With that, the transformation of $PbI_2$ to perovskite in presence of urea is promoted as evidenced in GI-XRD (Figures 3G and 3H) and BB-XRD (Figure 2D). Besides the chemical modulation of the crystallization process, the application of a low-temperature annealing process in the hybrid evaporation/spin-coating fabrication method has been previously demonstrated to enhance the $PbI_2$ to perovskite transformation owing to the reduced volatilization of organohalides.[25] Given the perovskite seeding growth mechanism with urea, which is compatible with the use of a low annealing temperature (100°C), more organohalide

molecules are expected to diffuse into the scaffold in contrast to volatilization at high temperature in the reference film (150°C). Together, the aforementioned mechanisms lead to a reduction of insulating $PbI_2$ at the perovskite/HTL bottom interface.

To understand the effect of urea treatment and the impact of remnant $PbI_2$ at the perovskite/2PACz interface on the hole extraction, we carried out transient surface photovoltage measurements (tr-SPV)[57,58] as shown in Figures 3I and 3J. The sample was excited with 1- and 10-sun equivalent laser fluences. The urea-treated perovskite/2PACz interface showed a faster rise of SPV at $10^{-8}$ s timescale in comparison to the reference (see 1 and 2 in Figure 3I), which indicates a faster hole extraction. The presence of shallow defects might explain the decelerated extraction in the reference perovskite.[59] Additionally, the higher SPV at later times ($10^{-5}$–$10^{-4}$ s, see 3 in Figure 3I) is possibly associated with detraping activity of defects typical for this timescale.[60] Measurements conducted with 10-sun equivalent laser fluence show a larger SPV amplitude at short timescale of $10^{-8}$ s (see 4 in Figure 3J) and less pronounced kink (see 5 vs. 6 in Figure 3J). This behavior implies a more efficient hole extraction as well as a higher number of extracted holes, in addition to a reduction of shallow trap density in the urea-treated perovskite film in comparison to the reference. The proposed reduction of defect density is in full agreement with the results of the PL measurements, showing an increase in trPL lifetime and PL intensity (Figures 2F and 2H). This further agrees with the reduced remnant $PbI_2$ at the perovskite/2PACz interface with urea treatment and thus substantiates the importance of pursuing full scaffold-to-perovskite conversion with the hybrid method for enhancing the optoelectronic property of the absorber.

### Urea working mechanism for perovskite/$C_{60}$ surface passivation

In a second step, we investigate the urea additive's impact on the perovskite surface property as well as its interaction with the top ETL $C_{60}$. We vary the concentration from 0 mg/mL (reference) to 5 mg/mL and study samples consisting of textured silicon/ITO/2PACz/perovskite with/without $C_{60}$ (labeled perovskite stack and $C_{60}$ stack, respectively). Figure 4A shows the extracted $iV_{OC}$ values from *PLQY* measurements. For the reference film, a substantial 110 mV drop in $iV_{OC}$ is observed when moving from the perovskite stack (1,208 mV) to the $C_{60}$ stack (1,100 mV), highlighting the severe non-radiative recombination loss at the interface.[26,27] However, upon addition of urea, (1) for all incorporated urea concentrations, the perovskite stack's $iV_{OC}$ is increased, reaching a maximum of 1,240 mV at 3 mg/mL, and (2) the $C_{60}$ stack's $iV_{OC}$ is incrementally improved from 1,100 mV in the absence of urea up to 1,190 mV with 5 mg/mL. Using spatially resolved PL imaging, we further confirm our findings and stress the homogeneous character of the optoelectronic enhancement (Figure S8). Similarly, trPL measurements on $C_{60}$ stacks show a significant rise of the fitted charge carrier lifetime from 30 ns (reference) to 162 ns with 5 mg/mL urea incorporation (Figure 4B). Altogether, the results demonstrate that besides the crystallization regulation function, urea also provides a surface passivation at the $C_{60}$ junction.

Seeking to disentangle the overall impact of urea on perovskite solar cells and separately quantify its benefits of tailored crystallization kinetics and interfacial passivation, we prepared reference perovskite films and applied a urea surface treatment (interlayer between perovskite and $C_{60}$). To do that, we dissolved 5 mg/mL of urea in EtOH and spin-coated a 100 µL volume dynamically on the reference perovskite stack (3,000 rpm for 20 s), followed by an annealing treatment in air for 10 min. From PL measurements of the treated samples, a slight reduction in $iV_{OC}$ can be noted in comparison to the reference stack (around 10 mV), thereby

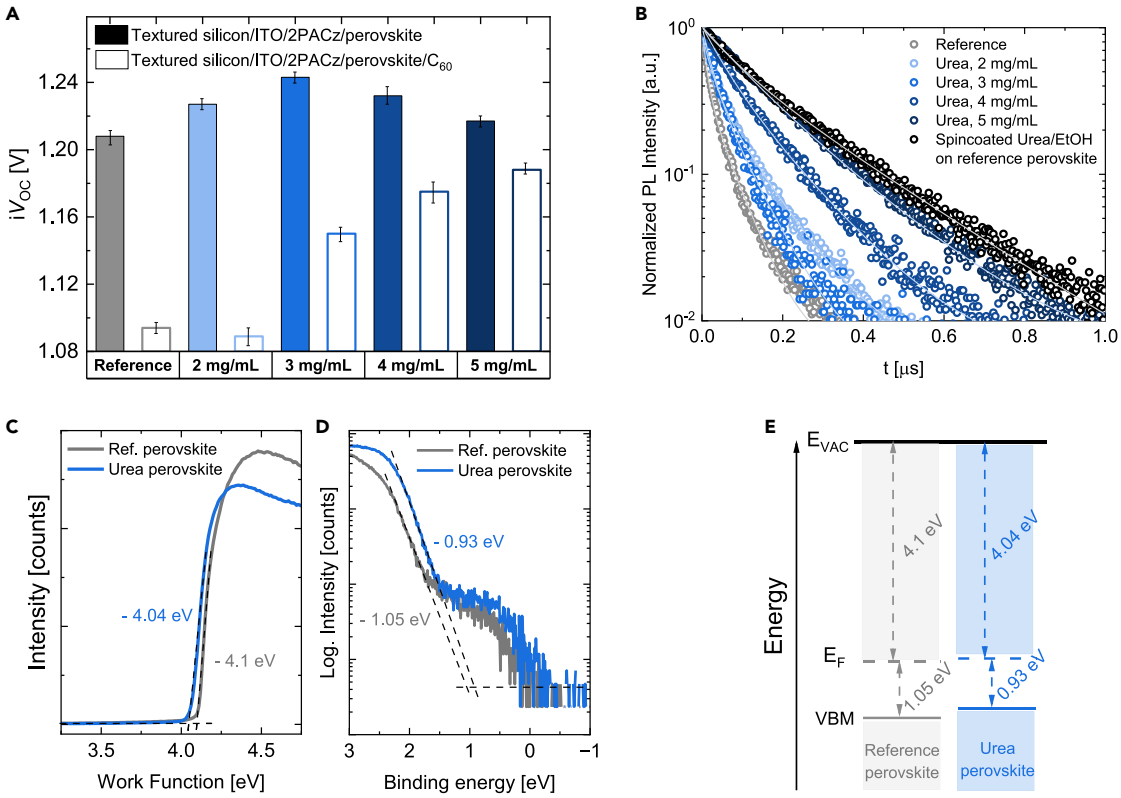


**Figure 4. Impact of urea on the perovskite/$C_{60}$ interfacial passivation**

(A) Implied open-circuit voltge ($iV_{OC}$) extracted from steady-state photoluminescence (PL) measurements realized on textured silicon/ITO/2PACz/perovskite stacks with/without $C_{60}$, where the perovskite absorber was treated with different concentrations of urea ranging from 2 to 5 mg/mL.
(B) Transient PL decays of textured silicon/ITO/2PACz/perovskite/$C_{60}$ stacks, with different urea concentrations in comparison to the reference.
(C and D) (C) Work function and (D) valence band maximum (VBM) derived from ultraviolet photoelectron spectroscopy (UPS) measurements on textured silicon/ITO/2PACz/perovskite stacks with/without urea (5 mg/mL).
(E) Constructed band diagram showing the Fermi level position and the VBM relative to vacuum ($E_{VAC}$).

underlining no chemical surface passivation (Figure S9). By contrast, upon addition of the $C_{60}$ layer, an 85 mV increase is observed for the urea-treated $C_{60}$ stack (1,180 mV) in comparison to the reference (1,095 mV). Furthermore, trPL measurements in Figure 4B show a further extension of the charge carrier lifetime to 174 ns (in comparison to 30 ns for reference), which highlights the surface passivation effect.

To understand the underlying mechanism of surface passivation in presence of urea, we investigate the perovskite's surface morphology. Top-view SEM images in Figures 5A–5D show the evolution of the perovskite surface as a function of urea concentration. Particularly, we observe that with increasing concentration, dark stripes with increasing size cover the top surface. Focusing on the 5 mg/mL films, AFM images (Figures 5H–5J) show that upon evaporation of $C_{60}$, the morphology of the stripes is still distinctly recognized, highlighting a local and physical separation between the absorber and the ETL (confirmed via SEM Figure S10). Because of carrier recombination and Fermi level pinning, a direct contact between perovskite and $C_{60}$ induces in-gap states that impair electronically the contact.[29,61] Therefore, the presence of organic molecules at the perovskite surface, locally displacing the $C_{60}$ layer, can effectively reduce the contact-induced gap states and enhance the interfacial passivation quality.

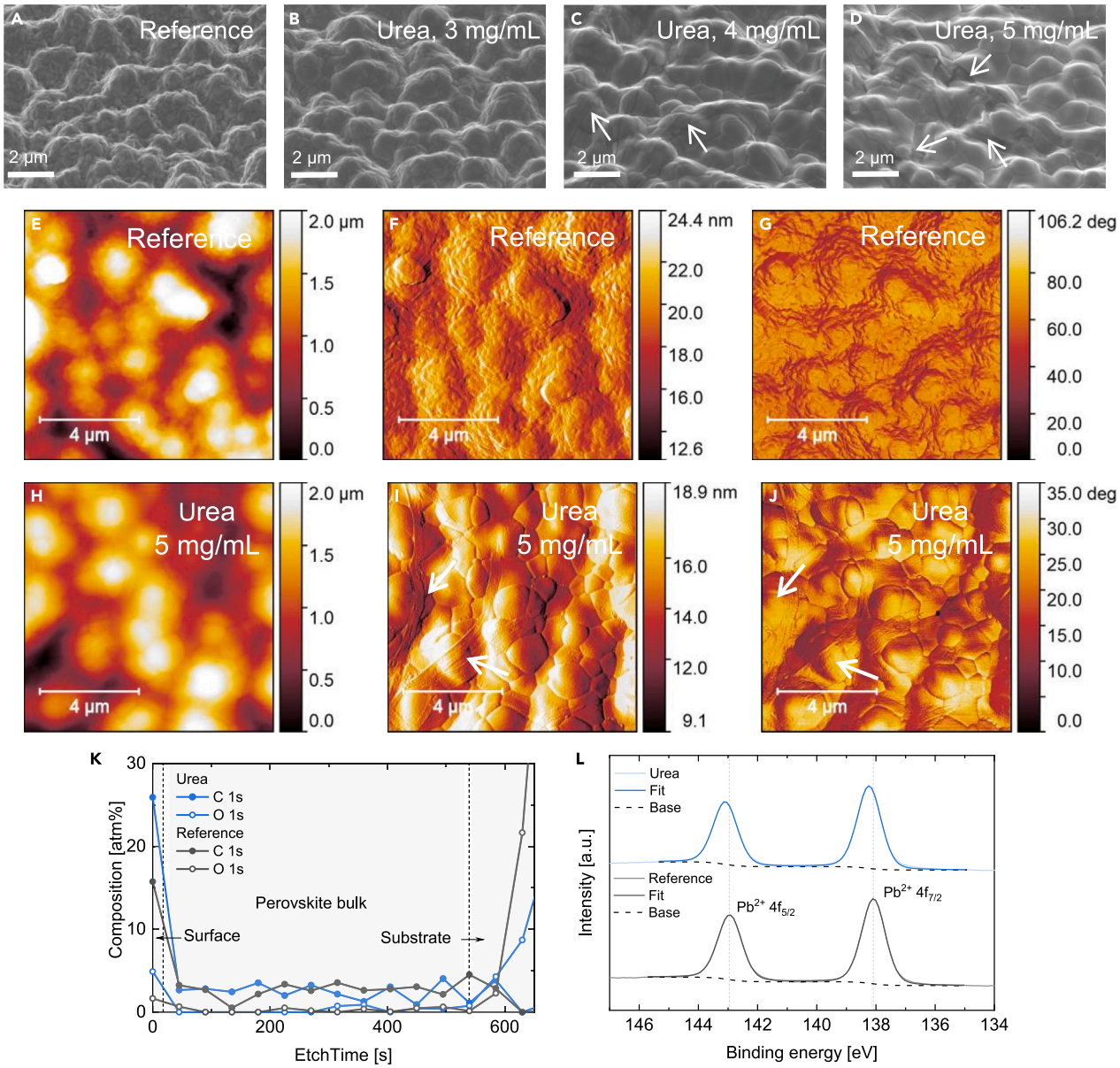


**Figure 5. Investigation of urea's impact on the perovskite surface morphology and composition**

(A–D) Top-view scanning electron microscopy (SEM) images of textured silicon/ITO/2PACz/perovskite stacks, with different urea concentrations, in comparison with the reference.

(E–J) Height (E and H), amplitude (F and I), and phase (G and J) images from atomic force microscopy (AFM) measurements of textured silicon/ITO/Perovskite/$C_{60}$ stacks.

(K) X-ray photoelectron spectroscopy (XPS) depth profiles showing carbon and oxygen signals of the perovskite absorbers (reference and urea treated) deposited on top of glass/ITO/2PACz substrates.

(L) XPS of Pb 4f core-level of reference and urea-treated perovskite absorbers.

X-ray photoelectron spectroscopy (XPS) measurements were carried out to investigate the composition of the organic molecules on the urea-treated perovskite top surface. Figures 5K and 5L show an XPS depth profile analysis on glass/ITO/2PACz/perovskite substrates (reference vs. urea with 5 mg/mL). With regard to oxygen, the only element of urea not present in any perovskite precursor used in this study, we found a three-fold increase in the atomic ratio at the surface of the urea-treated

perovskite in comparison to reference, as can be seen in Figure 5K (4.89 vs. 1.65 atm %), and confirmed at 2 other spots on the surface (Figure S11). Furthermore, the three-fold increase in oxygen atomic ratio was reproduced when performing measurements on textured silicon substrates (Figure S12). While we note that the measurement was carried out in air, which can affect the surface by carbon and oxygen contamination, the reproduced results confirm the oxygen enrichment in the urea-treated perovskite surface. With regard to potential Pb-coordination pathways, the detailed XPS spectra revealed a shift to higher binding energy of the Pb $4f_{5/2}$ and $4f_{7/2}$ peaks in urea-treated perovskite in comparison to reference (142.93 to 143.08 eV and 138.08 to 138.23 eV, respectively), which suggests a strong bonding between O and Pb (Figure 5L).[33,62] These observations were reproduced on textured substrates (Figure S12B). Similar to oxygen, a carbon enrichment was found on the surface of the urea-treated perovskite absorber (25.9 vs. 15.7 atm%). Beyond the surface, the depth profile analysis showed no oxygen detection in the perovskite bulk for both films, whereas the carbon level was comparable, which hints toward the absence of urea within the absorber's bulk, e.g., at grain boundaries. Using extracted data at 315 s etch time (Figure S13), the estimated bulk perovskite compositions are $Cs_{0.14}FA_{0.86}Pb(I_{0.77}Br_{0.23})_3$ for reference and $Cs_{0.14}FA_{0.86}Pb(I_{0.78}Br_{0.22})_3$ with urea treatment. We hypothesize that the slight decrease in Br with urea treatment is caused by the better infiltration of the modified FABr-FAI solution within the scaffold (homogeneous Br incorporation along the converted perovskite), in comparison to the reference case where a higher Br content is expected to be incorporated in the thinner "effectively" converted perovskite (this translates to a slight band-gap change as evidenced by the shift in PL peak position in Figure 2F).

Besides, we found that increasing the annealing temperature beyond the urea melting point (133°C)[63] leads to the absence of stripes on the surface (tested range: 100°C, 125°C, 150°C, and 175°C, Figure S14). Altogether, the results suggest that the formed discontinuous stripes on the perovskite surface are organic compounds that are most likely to stem from urea after perovskite crystallization and are responsible for the reduction of non-radiative recombination at the perovskite/$C_{60}$ interface via contact displacement.[29,61]

At 100°C (the used temperature in this study), we note that the expulsion of excess urea molecules takes place in the upward direction due its high volatility in comparison to the other compounds in the system. Adding to that, its big size, which does not fit in the perovskite crystal structure, makes it more favorable to be expelled from the lattice to accumulate at the surface. Furthermore, we observe that by applying a washing step of the urea-treated perovskite surface (with EtOH), excess urea molecules can be removed, as highlighted in SEM images in Figure S15B, leading to a drastic decrease in the tandem solar cell's $V_{OC}$ (Figure S15A). On the other hand, forming a continuous layer by spin-coating a solution of urea dissolved in EtOH on the reference perovskite lowers the tandem solar cell's performance due to the thickness and non-conductive nature of urea ($3–6 \times 10^{-8}$ S/cm).[64] This emphasizes the importance of having a thin and discontinuous layer for effective surface passivation.

Finally, using ultraviolet photoelectron spectroscopy measurements, we investigated the impact of urea on the energy level positions of the perovskite top surface (Figures 4C–4E). Treatment with urea results in a shifting of the valence band maximum (VBM) position of the perovskite upward toward vacuum (from 5.15 eV for the reference perovskite to 4.97 eV for the urea-treated perovskite). Consequently, the reduced energetic offset at the perovskite/$C_{60}$ interface contributes to further reducing the interfacial non-radiative recombination.

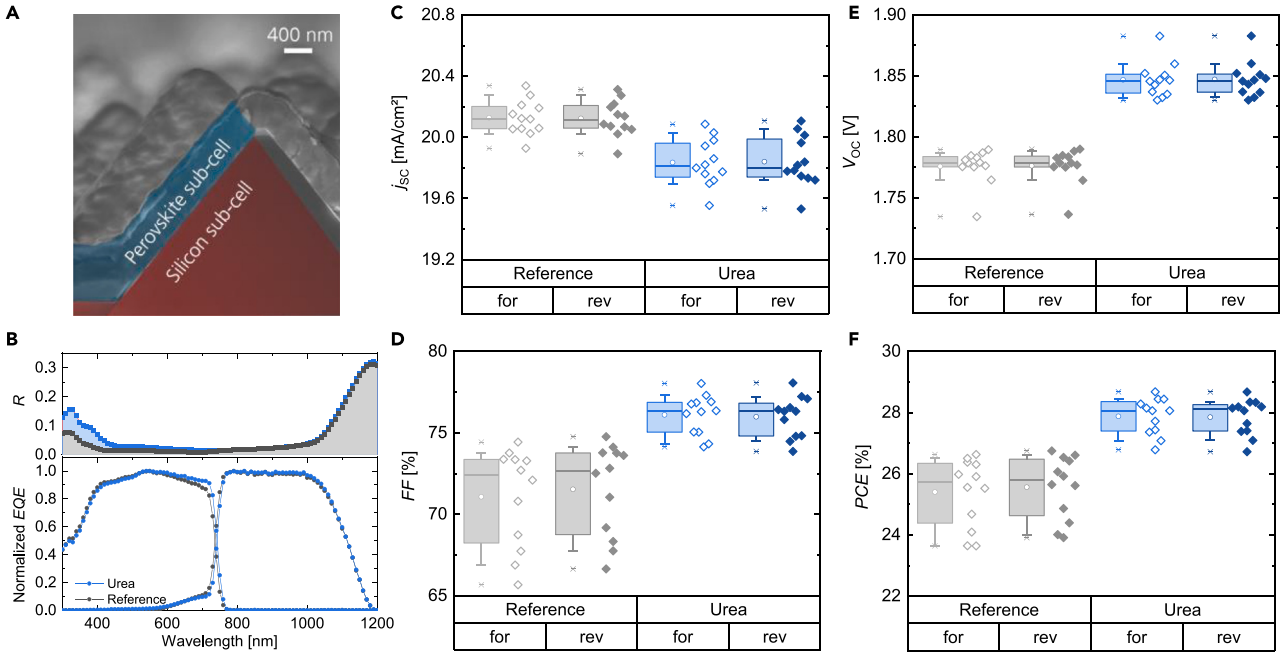


**Figure 6. Device characterization of fully textured perovskite silicon tandem solar cells**

(A) Cross-section scanning electron microscopy image of a tandem solar cell.

(B–F) (B) External quantum efficiency (*EQE*) and reflection (*R*) of representative devices with/without urea. Photovoltaic parameters presented in a box plot showing the (C) short-circuit current density ($j_{SC}$), (D) fill factor (*FF*), (E) open-circuit voltage ($V_{OC}$), and (F) power conversion efficiency (*PCE*) of fully textured perovskite silicon tandem solar cells with/without urea.

## FT-TSCs

To evaluate urea's dual crystallization and surface passivation function at low temperature on device level, we insert reference and urea-treated perovskite absorbers (5 mg/mL found as optimum as can be seen in Table S2) in a *p-i-n* perovskite top cell on top of a silicon heterojunction bottom cell (Figure 6A).

Statistical distribution of the photovoltaic parameters obtained for the devices are shown in Figures 6C–6F. Compared with reference devices, adding urea contributed to a substantial increase in $V_{OC}$ (+70 mV on average) and *FF* (+4.4%$_{abs.}$ on average), which led to a 2.4%$_{abs.}$ increase in the average *PCE* of FT-TSCs (25.7% to 28.1%) and higher reproducibility (standard deviation drops from 0.98%$_{abs.}$ to 0.56%$_{abs.}$). Nevertheless, we noted a slight decrease in the average $j_{SC}$ from 20.1 mA/cm$^2$ (reference) to 19.8 mA/cm$^2$ (with urea). The current density-voltage (*jV*) curves as well as photovoltaic performance metrics of the best devices are shown in Figures 7A and 7B.

On the one hand, the enhanced $V_{OC}$ reflects the suppressed non-radiative recombination losses mainly at the perovskite/$C_{60}$ interface as discussed in section urea working mechanism for perovskite/C60 surface passivation. By extending the voltage loss analysis study to incorporate the deposition of subsequent $SnO_x$ and ITO layers, Figure S16 shows that the i$V_{OC}$ of the perovskite top-cell stack with urea modification is enhanced from 1,070 mV (reference) to 1,140 mV, thereby reproducing the 70 mV increase in the final tandem device $V_{OC}$ (Figure 6E).

On the other hand, we attribute the main increase in *FF* to the perovskite's large grain size formation as well as reduced $PbI_2$ impurities at the perovskite/2PACz

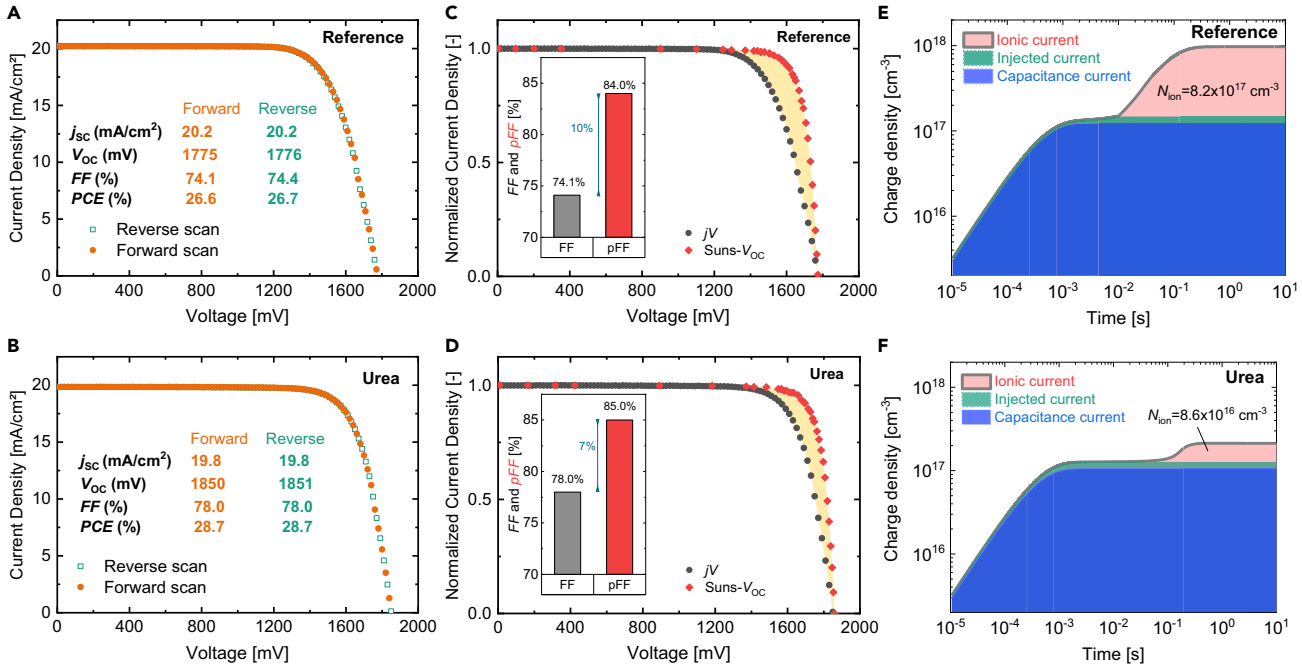


**Figure 7. Electrical characterization of champion devices and quantification of series resistance losses and mobile ion densities**

Current density-voltage (*jV*) measurements and photovoltaic parameters of champion fully textured perovskite silicon tandem solar cells (A) without urea (reference) and (B) with urea. Pseudo-*jV* and *jV* curves (reverse) of the champion devices (C) without and (D) with urea, to characterize series resistance losses. Charge density extracted by performing bias-assisted charge extraction (BACE) measurements on tandem devices (E) without urea (reference) and (F) with urea.

interface, which reduces the series resistance ($R_s$) experienced by charge carriers during transport and extraction. To quantify $R_s$, we performed Suns-$V_{OC}$ measurements on the champion devices. Figures 7C and 7D show that adding urea reduced the difference between the *FF* and pseudo-*FF* (pFF), which we attribute to a reduction in $R_s$ loss from ~10 to ~7 Ω cm$^2$. We note that the reduction in non-radiative recombination by the incorporation of urea also slightly increased the p*FF* by 1%$_{abs}$., thus effectively reducing the non-radiative recombination *FF* loss, with respect to the radiative limit. To further gain insight on the *FF* losses associated with non-radiative recombination, we carried out PL-based implied *FF* (iFF) imaging on the perovskite sub-cell stack with textured silicon as a substrate (here Si is not photoactive and is rather used as a substrate to provide the textured morphology). For i*FF* imaging, the illumination intensity is varied, and the detected PL images are converted to i$V_{OC}$ images for each illumination intensity. This set of i$V_{OC}$ images corresponds to a spatially resolved Suns-PL measurement. From this, i*FF* images can be calculated. Figure S17 shows that with urea incorporation, a 3.4%$_{abs.}$ increase in global i*FF* can be obtained (from 84.3% to 87.7%, based on a global suns-PL curve extracted from averaged i$V_{OC}$ images), which highlights the suppression of non-radiative recombination losses and enhancement of the *QFLS* in the perovskite sub-cell of the target tandem device.

To investigate the origin of reduced $j_{SC}$ with urea, external quantum efficiency (*EQE*) and reflection measurements were carried out (Figure 6B). The reflection spectrum presented a higher reflection pattern in the 280–450 nm range. The increased reflection loss in urea-treated tandem solar cells can be explained by the smoothening of the texture as displayed in the SEM images as well as the reflection pattern

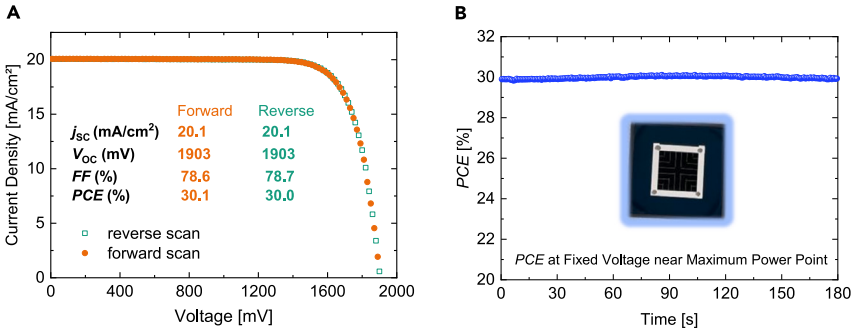


**Figure 8. Electrical characterization of urea-treated perovskite silicon tandem device with optimized contact layers**

(A) Current density-voltage (*jV*) measurements and photovoltaic parameters of an optimized fully textured perovskite silicon tandem solar cell with urea incorporation, increased 2PACz annealing temperature (125°C instead of 100°C), and $SnO_x$ buffer layer thickness (30 nm instead of 20 nm).
(B) Stabilized power conversion efficiency at a fixed voltage near maximum power point of the device. The device delivers 30.0% stabilized *PCE*.

of FT-TSCs (Figure S18). From this perspective, future work should focus on the utilization of larger silicon pyramid heights (3–4 μm) to restore perovskite conformality in the presence of crystallization additives. Besides increased reflection, the slight reduction in perovskite band gap with urea (1.66 eV instead of 1.67 eV) increases the photogenerated current in the perovskite sub-cell and reduces it in the silicon sub-cell. As the reference tandem device is silicon-limited with regard to the current-matching point,[10] in presence of urea, the photogenerated current in the silicon sub-cell is further reduced.

We note that for reference devices, a light-soaking period of around 60–90 min where devices were kept at open-circuit condition under 1-sun illumination was required to reach the stabilized efficiency, while this was not needed for devices with urea treatment. After stabilization, the power output recorded by applying a fixed voltage close to the maximum power point for all devices in the batch was stable for 90 s (Figure S19) and matched the efficiency extracted from the reverse *jV* curves plotted in Figure 6F. We ascribe the need for photoactivation in reference devices to a higher mobile ion density in the perovskite film. To confirm the hypothesis, we performed bias-assisted charge extraction (BACE) measurements (previously demonstrated for single-junction perovskite solar cells).[65,66] Figures 7E and 7F show that the addition of urea effectively reduces the mobile ion density by nearly one order of magnitude ($8.2 \times 10^{17}$ to $8.6 \times 10^{16}$ $cm^{-3}$), thus rationalizing the suppressed light-soaking phenomenon.

We carried out a long-term stability test on tandem devices in the dark in an $N_2$-rich atmosphere. The devices showed a comparable decay pattern over the 6,000-h duration (Figure S20). Furthermore, we tested the perovskite absorber's intrinsic stability under environmental stressors (temperature, humidity, and light). The 800-h testing period did not reveal severe degradation patterns as shown in Figure S21.

By further optimizing the perovskite sub-cell's functional layers (increased 2PACz annealing temperature from 100°C to 125°C for more robust SAM formation and $SnO_x$ buffer layer thickness from 20 nm to 30 nm for better protection from ITO sputter damage), a FT-TSC with incorporated urea delivered 30.0% *PCE* (Figure 8). A certified stabilized *PCE* at Fraunhofer ISE CalLab reached 28.54% (Figures S22 and S23). The demonstration for the use of a low annealing temperature process at 100°C for

FT-TSCs (Table S1 in supplemental information) opens the path for investigation of more temperature-sensitive and scalable CTLs.

### Conclusions

Incorporated in the solution step within the hybrid evaporation/spin-coating perovskite deposition method, urea allows a simultaneous regulation of the crystallization process and a passivation of the perovskite/$C_{60}$ interface, thereby tackling both main issues of non-ideal $V_{OC}$ and *FF* in industry-compatible fully textured perovskite silicon tandems. Through a series of investigations, we propose that the Lewis base nature of urea enables as a coordination with the $PbI_2$ precursor, which reduces the energy barrier for the perovskite $\alpha$-phase formation (prior to the annealing step). The presence of seeds at room temperature enables crystal growth commencement directly from these seeds during the annealing step, which leads to the growth of large crystalline domains. As a result, the perovskite apparent grain size is promoted to >1 μm, the bulk radiative quality is enhanced, the crystallinity is improved, and the mobile ion density is reduced. Furthermore, by controlling the additive's concentration, remnant urea molecules are expelled to the top surface, thereby forming a physical/electrical separation with the top $C_{60}$ layer and passivating the traps at that interface. Together with a reduced annealing temperature, which enhances the $PbI_2$ to perovskite conversion, the combination of these effects enables a $2.4\%_{abs.}$ average increase in the PCE of FT-TSCs with urea in comparison to reference devices. By optimizing functional layers, we achieve a *PCE* of 30.0% on 1 $cm^2$ device active area. This work provides new insights on perovskite formation on large pyramid texture and proposes a method paving the way for high-performance and industry-compatible perovskite silicon tandem solar cells.

## EXPERIMENTAL PROCEDURES

### Resource availability

#### *Lead contact*

Further information and requests for resources and materials should be directed to and will be fulfilled by the lead contact, Oussama Er-raji (Oussama.er-raji@ise.fraunhofer.de)

#### *Materials availability*

This study did not generate new, unique materials.

#### *Data and code availability*

The data that support the findings of this study are available from the corresponding author upon reasonable request.

### Silicon-bottom cell fabrication

Silicon solar cells were fabricated from 250 μm thick p-doped silicon wafers (float zone) with 1 ohm cm base resistivity purchased from Siltronic. Using potassium hydroxide (KOH), a pyramidal texture was etched on both sides of the wafer, yielding a pyramid size distribution ranging from 1 to 4 μm as derived from LEXT optical microscope images (Figure S24). Next, an RCA cleaning was applied to clean the silicon surface. Using plasma-enhanced chemical vapor deposition (PECVD) in an Indeotec cluster tool, a stack consisting of intrinsic/doped amorphous silicon passivation layers was subsequently deposited on both sides. The parallel-plate PECVD reactor was powered at 13,560 kHz at 200°C using a gas mixture of hydrogen ($H_2$), trimethylboron (TMB), silane ($SiH_4$), and phosphine ($PH_3$). The thickness of the p-doped and n-doped layers was set to 12 nm, while the thickness of the intrinsic layers was set to 6 nm. Next, the recombination layer was formed through a 1 $cm^2$

shadow mask on the front silicon side via DC sputtered ITO ($In_2O_3/SnO_2$ = 90/10 wt %) in an Oxford Instruments cluster tool using a mixture of oxygen and argon. Prior to ITO and amorphous silicon deposition, a dipping treatment (aqueous solution of 1% hydrogen fluoride) was carried out to eliminate silicon oxide ($SiO_2$) from the surface. On the back silicon side, a 195 nm ITO layer was sputtered on the full area. The rear contact was subsequently formed via a 1,000 nm thick silver layer. Finally, the 4-inch wafers were lasered in 2.5 × 2.5 $cm^2$ large substrates. Each substrate contains one 1 × 1 cm ITO pad (recombination layer) to build one tandem solar cell.

### Perovskite top-cell fabrication

Perovskite sub-cells were fabricated in the *p-i-n* structure. Firstly, a surface cleaning procedure consisting of dynamically spin-coating a 200 μL volume of ethanol (EtOH) at 2,500 rpm for 30 s was performed to remove silicon particles that might stem from the laser breaking procedure. Then, the samples were subjected to a UV/ozone treatment for 15 min to eliminate contaminants from the surface. The hole transport layer (HTL) was subsequently formed by statically spin-coating (7 s waiting time, 3,000 rpm, 30 s) a 100 μL volume of a 7 mmol 2PACz (self-assembling monolayer from Dyenamo) solution prepared in EtOH. Subsequently, a thermal annealing step at 100°C (125°C for champion device) for 10 min was applied to ensure the conformal binding between the phosphonic group of the self-assembling monolayer and the ITO recombination layer. We note that the 2PACz solution vial was pre-treated by ultrasonication for 15 min at room temperature prior to usage (during the same time as the samples were in the UV/ozone tool). Furthermore, we use a highly concentrated 2PACz solution (standard in the community is 1 mmol) for better reproducibility on textured silicon. Next, we deposit the perovskite absorber using the hybrid evaporation/spin-coating route. In a first step, CsI (powder from Sigma-Aldrich) and $PbI_2$ (beads from Alfa Aesar) were thermally co-evaporated from ceramic crucibles to form a 550 nm thick inorganic template in a Lesker mini Spectros system. The evaporation rates of CsI and $PbI_2$ were set to 0.1 Å/s (reached at ~400°) and 1 Å/s (reached at ~280°C), respectively, and were measured via quartz crystal balances. Furthermore, the evaporation started at a base pressure < 2 × $10^{-6}$ Torr, and the substrate temperature was set to 20°C. In a second step, 0.67 M solutions of FABr and FAI (from Dyenamo) were prepared in EtOH (from ROTH, purity > 99.8%) and added after ~8 h to give a FABr/FAI mixture of 65/35 vol %. For perovskite films with urea, unless differently specified, 5 mg/mL of urea was added to the FABr/FAI solution. The solutions were stirred overnight. On the next day, a 150 μL volume of the organohalide solution was dynamically spin-coated on the pre-evaporated scaffold (2,200 rpm, 35 s) followed by an annealing treatment in air. If not specified in the text, reference perovskite films (i.e., with no urea incorporation) were annealed at 150°C for 25 min, while perovskite films with urea were annealed at 100°C for 10 min. To form the electron transport layer (ETL), a 21 nm thick $C_{60}$ (from TCI) layer was evaporated (evaporation rate ~0.15 Å/s measured by a quartz crystal sensor, evaporation temperature ~470°C, base pressure < 4 × $10^{-6}$ Torr). Then, the 20 nm (30 nm for champion device) buffer layer was ensured by atomic layer deposition of $SnO_x$ at 80°C. As precursors, de-ionized water (kept at room temperature) and tetrakis(dimethylamino)tin(IV) (TDMASn, kept at 50°C) were used. The doses and purge times were 0.3/1/0.2/10 s for TDMASn/purge/$H_2O$/purge. Following that, a 20 nm thick ITO window layer was DC sputtered through a shadow mask. The front contact was then formed via a 200 nm thick Ag layer (5 Å/s evaporation rate measured by quartz crystal balance, 5 × $10^{-6}$ Torr base pressure) using a shadow mask to define the 1 $cm^2$ active area. Finally, a 100 nm thick antireflective coating was deposited via thermal evaporation (2 Å/s evaporation rate measured by quartz crystal balance, 5 × $10^{-6}$ Torr base pressure).

Note that for thermally evaporated layers, the thickness values are given for a flat substrate. The measured thickness on the pyramid size is lower due to the increased surface area (texture factor of ~1.4).

## Materials characterization

### *SEM measurements*

Cross-sectional and top-view electron microscopy images were captured using a Zeiss device with a Schottky emission SEM (model Auriga 60, In lens detector). The acceleration voltage was set to 5 kV. The top-view images were taken with an angle of 45°.

### *AFM measurements*

Atomic force microscopy (AFM) measurements were performed in tapping mode using a FastScan Dimension XR AFM (Bruker) with RTESPA-525 probes (Bruker). Images were recorded at 512 × 512 pixels. Basic image processing was performed in Gwyddion using various Gwyddion processes to align and level data.

### *XRD*

A Bruker D8 Advance diffractometer, equipped with a Cu anode at 40 mA/40 kV was used to perform X-ray diffraction (XRD) measurements. The step size was set at 0.3° and the time per step 0.1 s. The software DIFRAC.EVA was used to analyze the data.

### *XPS measurements*

X-ray photoelectron spectroscopy (XPS) was performed using a Surface Science Instruments S-probe spectrometer (with upgraded detector) with monochromatized Al Kα radiation at 10 000 eV acting as excitation source. The spot size was set to an area of 250 × 185 μm.

### *UPS measurements*

Ultraviolet photoelectron spectroscopy (UPS) measurements were performed using a Kratos Axis Ultra DLD spectrometer with a base pressure of $<1 \times 10^{-10}$ mbar and a He I α light source.

### *TrPL*

To measure transient photoluminescence (TrPL) decay, the samples were excited with a 515 nm diode laser (7.5 mm spot size diameter). Steady-state conditions of the charge carriers were ensured by setting the pulse width to 240 μs. The on/off ratio of the laser was 106 within 1 ns, with the transient being recorded during the off-time. During on time, the laser power was adjusted to match the $j_{SC}$ of a perovskite solar cell under 1-sun illumination (AM 1.5G). A VIS hybrid photodetector, which is read out using a single-photon counting device, was used to record the PL. The integration time was set to 300 s.

To extract the charge carrier lifetime $\tau$ for textured silicon/2PACz/perovskite half-stacks, a mono-exponential fit ($Y(t) = Ae^{-\frac{t}{\tau}}$) was applied. For silicon/2PACz/perovskite/$C_{60}$ half-stacks, a bi-exponential fit was applied ($Y(t) = A_1 e^{-\frac{t_1}{\tau_1}} + A_2 e^{-\frac{t_2}{\tau_2}}$) and the average lifetime was calculated following the equation ($\tau = A_1 \times \tau_1 + A_2 \times \tau_2$).

### *Spectrally resolved PL measurements*

Steady-state PL measurements were performed using a LUQY Pro instrument from Quantum Yield Berlin (QYB). The tool is equipped with a 532 nm laser. For measurements, the laser spot size was set to 3 s and the resolution time to 0.1 $cm^2$. The equivalent laser intensity was varied from 0.05 sun to 1 sun for intensity-dependent i$V_{OC}$

estimation (automatically calculated for the selected spot size as well as $j_{SC}$ and EQE at 532 nm).

### *PL-based i$V_{OC}$ imaging*

To acquire PL images, a measurement system built by Intego GmbH and developed at Fraunhofer ISE was used. A calibration of the measurement system allows to measure absolute PL images and convert them to i$V_{OC}$ images. To access the perovskite silicon tandem sub-cells selectively, two lasers with 450 and 808 nm wavelengths were used. Before acquiring an image of the perovskite sub-cells, a stabilization time (continuous illumination at open-circuit conditions) was set for the samples to reach their stabilized state. The method is described in more detail in Fischer et al. in the following reference.[40]

### *PL-based iFF imaging*

i*FF* images are extracted from a series of i$V_{OC}$ images acquired at different illumination intensities. Averaging the individual i$V_{OC}$ images allows to determine a global Suns-PL curve. From this curve, global i*FF* can be determined.

### *Transient surface photovoltage*

Measurements were conducted using a custom-built setup. The exposed perovskite surface was excited employing a tunable pumped pulse laser (Nd:YAG, EKSPLA, NT230-50) operating at 496 nm wavelength with a pulse duration of 5 ns and a frequency of 2 Hz. 20 curves were acquired and averaged. Transients were captured utilizing an oscilloscope card (Gage, CSE 1622–4GS, 200 MS/s) with software developed in-house for logarithmic data acquisition. The sample structure used in this work featured a 30 nm thin $Al_2O_3$ interlayer in order to decouple signals from silicon and perovskite, thus allowing for a better interpretation of the perovskite signal.

### *Suns-$V_{OC}$ measurements*

The measurements were conducted on the same measurement system that was also used for i$V_{oc}$ imaging. The lasers with distinct wavelengths of 450 and 808 nm enabled a sub-cell selective excitation. To measure the $V_{OC}$ at different illumination intensities, a source meter was electrically connected to the cell. By varying the illumination intensity and measuring $V_{OC}$, pseudo-*jV* curves were measured.

### *BACE*

The bias-assisted charged extraction (BACE) measurement was carried out similarly to the procedure reported by Thiesbrummel.[66] The device is initially held at a forward bias close to the $V_{OC}$ of a solar cell under illumination (IviSUN light source having an intensity of 100 klux) so that the injected current is similar to the $I_{SC}$. After stabilization time of 40 s, the bias was set to 0 V and the current was collected. For obtaining only the current extracted from the cell capacitance, the measurement was done symmetrically by switching from 0 V to a reverse bias close to the $V_{OC}$. The bias was applied to a solar cell via IVIUM compactstat. The collected current was measured through a 40 ohm shunt resistor and recorded via an oscilloscope (Picoscope 5000) with a time resolution up to 100 ns. The total charge density was obtained by integrating the current transient.

### *jV measurements*

A Wacom solar simulator equipped with two filtered light sources (halogen and xenon lamps) was used to perform current density-voltage (*jV*) measurements. The spectral response of a cell from each variation was measured prior to the *jV* measurements. With that, lamp intensities were calculated following the procedure described

by Meusel et al.[67] and adjusted using two filtered WPVS reference solar cells. In a next step, *jV* curves were recorded using a Keithly 2400 source meter in the range (−100, 1,900 mV) with a 34 mV/s scan speed and 20 mV step width in forward and then reverse direction. Between the single measurement points of the *jV* curve, the solar cell is under open-circuit condition. The measurements are carried out in air with a temperature-controlled stage set at 25°C. A shadow mask was used to limit light exposure area to the 1 $cm^2$ cell active area.

### *EQE*

The external quantum efficiency was measured as described in our previous publication.[68] Note that the measured EQEs are not absolute. Details can be found in Bett et al.[69]

### *Reflection*

Reflection measurements on tandem solar cells were carried out in a LOANA tool from PvTools. A monochromatic light from xenon and tungsten lamps was used with a spot size of 3 × 5 mm. The reflectance is measured under an 8° tilt with a BaSO4-coated integrating sphere.

## SUPPLEMENTAL INFORMATION

Supplemental information can be found online at https://doi.org/10.1016/j.joule.2024.06.018.

## ACKNOWLEDGMENTS

This work was funded by the Fraunhofer LIGHTHOUSE PROJECT MaNiTU as well as the German Federal Ministry for Economic Affairs and Climate Action under contract no. 03EE1086A (PrEsto) as well as 03EE1087A and 03EE1087B (KATANA). We thank E. Köhnen for insightful discussions on tr-SPV, J. Zielonka for her support with SEM measurements, F. Martin for the support with reflection measurements, K. Aborov and A. Gonzalez Abad for the support with EQE measurements, K. Zimmermann and H. Nagel for silicon-bottom solar cell processing, and K. Fischer and J. Myers for technical support. A.J.R. acknowledges the Henry Royce Institute for Advanced Materials, funded through EPSRC grants EP/R00661X/1, EP/S019367/1, EP/P02470X/1, and EP/P025285/1, for the Bruker Dimension XR access at the University of Sheffield. A.M. acknowledges financial funding from the European Union HORIZON-MSCA-2021-PF-01-01 under grant agreement no. 101061809 (HyPerGreen) and HyPerCells support (a joint graduate school of the University of Potsdam and the Helmholtz-Zentrum Berlin).

## AUTHOR CONTRIBUTIONS

O.E. conceived the idea, designed, and performed the main experiments (fabricated the tandem devices, performed *jV*, intensity-dependent *PLQY*, trPL, BB-XRD, and GI-XRD measurements, as well as long-term stability tests), and wrote the manuscript. M.A.A.M. contributed to the experimental planning, performed experiments for the optimization of the deposition parameters with additive treatment, fabricated several film stacks presented in the manuscript and characterized them with XRD measurements, and provided important insights during data evaluation. O.F. performed Suns-$V_{OC}$ measurements, PL-based i$V_{OC}$ and i*FF* imaging measurements, and evaluated the data. T.W.G. carried out the tr-SPV measurements, and T.W.G. and A.M. evaluated the data. A.J.R. performed UPS and AFM measurements and evaluated the data. A.R. and A.S. performed XPS measurements and evaluated the data. D.B. performed BACE measurements and evaluated the data. Furthermore, D.B. made the schematics in Figure 1. M.B. provided silicon-

bottom solar cells and provided deep insight into understanding the tandem solar cell data. B.P.K. participated to important discussions for optimization of deposition parameters and fabricated multiple devices to ensure reproducibility. O.S.-W., M.H., M.C.S., J.B., and S.W.G. provided the funding (PrEsto, MaNiTU, and KATANA) as well as deep insight into the understanding of characterization data. P.S.C.S. supervised the project and gave essential suggestions about the experimental planning, conceptualization, and structure of the manuscript. All authors reviewed the manuscript and repeatedly helped with manuscript reviews.

## DECLARATION OF INTERESTS

O.E., M.A.A.M., O.S.-W., J.B., and P.S.C.S. are inventors on a provisional patent related to the subject matter of this manuscript (patent file number DE 10 2024 104 351.2.).

Received: January 30, 2024
Revised: March 20, 2024
Accepted: June 20, 2024
Published: July 19, 2024

## REFERENCES

1. Zafoschnig, L.A., Nold, S., and Goldschmidt, J.C. (2020). The Race for Lowest Costs of Electricity Production: Techno-Economic Analysis of Silicon, Perovskite and Tandem Solar Cells. IEEE J. Photovoltaics *10*, 1632–1641.

2. Chang, N.L., Zheng, J., Wu, Y., Shen, H., Qi, F., Catchpole, K., Ho-Baillie, A., and Egan, R.J. (2021). A bottom-up cost analysis of silicon–perovskite tandem photovoltaics. Progress in Photovoltaics *29*, 401–413.

3. Messmer, C., Goraya, B.S., Nold, S., Schulze, P.S., Sittinger, V., Schön, J., Goldschmidt, J.C., Bivour, M., Glunz, S.W., and Hermle, M. (2021). The race for the best silicon bottom cell: Efficiency and cost evaluation of perovskite–silicon tandem solar cells. Prog. Photovolt. *29*, 744–759.

4. Sofia, S.E., Wang, H., Bruno, A., Cruz-Campa, J.L., Buonassisi, T., and Peters, I.M. (2020). Roadmap for cost-effective, commercially-viable perovskite silicon tandems for the current and future PV market. Sustainable Energy Fuels *4*, 852–862.

5. Li, Z., Zhao, Y., Wang, X., Sun, Y., Zhao, Z., Li, Y., Zhou, H., and Chen, Q. (2018). Cost Analysis of Perovskite Tandem Photovoltaics. Joule *2*, 1559–1572.

6. Callies, A., Hanser, M., Goldschmidt, J.C., Bläsi, B., and Höhn, O. (2023). Structuring of perovskite-silicon tandem solar cells for reduced reflectance and thermalization losses. Opt. Express *31*, 19428–19442.

7. Jäger, K., Sutter, J., Hammerschmidt, M., Schneider, P.-I., and Becker, C. (2021). Prospects of light management in perovskite/silicon tandem solar cells. Nanophotonics *10*, 1991–2000.

8. Xu, Q., Zhao, Y., and Zhang, X. (2019). Light Management in Monolithic Perovskite/Silicon Tandem Solar Cells. Sol. RRL *173*, 1900206.

9. Hossain, M.I., Qarony, W., Jovanov, V., Tsang, Y.H., and Knipp, D. (2018). Nanophotonic design of perovskite/silicon tandem solar cells. J. Mater. Chem. A *6*, 3625–3633.

10. Er-Raji, O., Messmer, C., Bett, A.J., Fischer, O., Reichmuth, S.K., Schindler, F., Bivour, M., Schultz-Wittmann, O., Borchert, J., Hermle, M., et al. (2023). Loss Analysis of Fully-Textured Perovskite Silicon Tandem Solar Cells: Characterization Methods and Simulation toward the Practical Efficiency Potential. Sol. RRL *7*, 2300659.

11. Mariotti, S., Köhnen, E., Scheler, F., Sveinbjörnsson, K., Zimmermann, L., Piot, M., Yang, F., Li, B., Warby, J., Musiienko, A., et al. (2023). Interface engineering for high-performance, triple-halide perovskite–silicon tandem solar cells. Science *381*, 63–69.

12. Aydin, E., Ugur, E., Yildirim, B.K., Allen, T.G., Dally, P., Razzaq, A., Cao, F., Xu, L., Vishal, B., Yazmaciyan, A., et al. (2023). Enhanced optoelectronic coupling for perovskite-silicon tandem solar cells. Nature *623*, 732–738.

13. Schulze, P.S.C., Wienands, K., Bett, A.J., Rafizadeh, S., Mundt, L.E., Cojocaru, L., Hermle, M., Glunz, S.W., Hillebrecht, H., and Goldschmidt, J.C. (2020). Perovskite Hybrid Evaporation/Spin Coating Method: From Band Gap Tuning to Thin Film Deposition on Textures. Thin Solid Films *704*, 137970.

14. Sahli, F., Werner, J., Kamino, B.A., Bräuninger, M., Monnard, R., Paviet-Salomon, B., Barraud, L., Ding, L., Diaz Leon, J.J., Sacchetto, D., et al. (2018). Fully textured monolithic perovskite/silicon tandem solar cells with 25.2% power conversion efficiency. Nat. Mater. *17*, 820–826.

15. Nogay, G., Sahli, F., Werner, J., Monnard, R., Boccard, M., Despeisse, M., Haug, F.-J., Jeangros, Q., Ingenito, A., and Ballif, C. (2019). 25.1%-Efficient Monolithic Perovskite/Silicon Tandem Solar Cell Based on a p -type Monocrystalline Textured Silicon Wafer and High-Temperature Passivating Contacts. ACS Energy Lett. *4*, 844–845.

16. Luo, X., Luo, H., Li, H., Xia, R., Zheng, X., Huang, Z., Liu, Z., Gao, H., Zhang, X., Li, S., et al. (2023). Efficient Perovskite/Silicon Tandem Solar Cells on Industrially Compatible Textured Silicon. Adv. Mater. *35*, e2207883.

17. Li, Y., Shi, B., Xu, Q., Yan, L., Ren, N., Chen, Y., Han, W., Huang, Q., Zhao, Y., and Zhang, X. (2021). Wide Bandgap Interface Layer Induced Stabilized Perovskite/Silicon Tandem Solar Cells with Stability over Ten Thousand Hours. Adv. Energy Mater. *11*, 2102046.

18. Xu, Q., Shi, B., Li, Y., Yan, L., Duan, W., Li, Y., Li, R., Ren, N., Han, W., Liu, J., et al. (2022). Conductive Passivator for Efficient Monolithic Perovskite/Silicon Tandem Solar Cell on Commercially Textured Silicon. Adv. Energy Mater. *12*, 2202404.

19. Yan, L., Li, Y., Shi, B., Li, Y., Xu, Q., Zhang, B., Chen, Y., Han, W., Ren, N., Huang, Q., et al. (2022). Reducing electrical losses of textured monolithic perovskite/silicon tandem solar cells by tailoring nanocrystalline silicon tunneling recombination junction. EuroSun2004 *245*, 111868.

20. He, Y., Tang, Z., He, B., Han, C., Ding, L., Gu, X., Zhang, Y., Yan, H., and Xu, X. (2023). Composition engineering of perovskite absorber assisted efficient textured monolithic perovskite/silicon heterojunction tandem solar cells. RSC Adv. *13*, 7886–7896.

21. Mao, L., Yang, T., Zhang, H., Shi, J., Hu, Y., Zeng, P., Li, F., Gong, J., Fang, X., Sun, Y., et al. (2022). Fully Textured, Production-Line Compatible Monolithic Perovskite/Silicon Tandem Solar Cells Approaching 29% Efficiency. Adv. Mater. *34*, e2206193.

22. Zhang, F., Tu, B., Yang, S., Fan, K., Liu, Z., Xiong, Z., Zhang, J., Li, W., Huang, H., Yu, C., et al. (2023). Buried-Interface Engineering of Conformal 2D/3D Perovskite Heterojunction

for Efficient Perovskite/Silicon Tandem Solar Cells on Industrially Textured Silicon. Adv. Mater. *35*, e2303139.

23. Chin, X.Y., Turkay, D., Steele, J.A., Tabean, S., Eswara, S., Mensi, M., Fiala, P., Wolff, C.M., Paracchino, A., Artuk, K., et al. (2023). Interface passivation for 31.25%-efficient perovskite/silicon tandem solar cells. Science *381*, 59–63.

24. Sun, Y., Mao, L., Yang, T., Zhang, H., Shi, J., Tan, Q., Li, F., Zeng, P., Gong, J., Liu, Z., and Liu, M. (2023). Ionic Liquid Modified Polymer Intermediate Layer for Improved Charge Extraction toward Efficient and Stable Perovskite/Silicon Tandem Solar Cells. Small *20*, e2308553.

25. Er-Raji, O., Rustam, L., Kore, B.P., Glunz, S.W., and Schulze, P.S.C. (2023). Insights into Perovskite Film Formation Using the Hybrid Evaporation/Spin-Coating Route: An In Situ XRD Study. ACS Appl. Energy Mater. *6*, 6183–6193.

26. Warby, J., Zu, F., Zeiske, S., Gutierrez-Partida, E., Frohloff, L., Kahmann, S., Frohna, K., Mosconi, E., Radicchi, E., Lang, F., et al. (2022). Understanding Performance Limiting Interfacial Recombination in pin Perovskite Solar Cells. Adv. Energy Mater. *12*, 2103567.

27. Stolterfoht, M., Caprioglio, P., Wolff, C.M., Márquez, J.A., Nordmann, J., Zhang, S., Rothhardt, D., Hörmann, U., Amir, Y., Redinger, A., et al. (2019). The impact of energy alignment and interfacial recombination on the internal and external open-circuit voltage of perovskite solar cells. Energy Environ. Sci. *12*, 2778–2788.

28. Caprioglio, P., Zu, F., Wolff, C.M., Márquez Prieto, J.A., Stolterfoht, M., Becker, P., Koch, N., Unold, T., Rech, B., Albrecht, S., et al. (2019). High open circuit voltages in pin-type perovskite solar cells through strontium addition. Sustainable Energy Fuels *3*, 550–563.

29. Liu, J., de Bastiani, M., Aydin, E., Harrison, G.T., Gao, Y., Pradhan, R.R., Eswaran, M.K., Mandal, M., Yan, W., Seitkhan, A., et al. (2022). Efficient and stable perovskite-silicon tandem solar cells through contact displacement by MgFx. Science *377*, 302–306.

30. Fiala, P.J. (2022). Material Development for Perovskite/Silicon Tandem Photovoltaics. PhD. thesis (EPFL)).

31. Li, Y., Wang, X., Xu, Q., Li, Y., Zhang, Y., Han, W., Sun, C., Zhu, Z., Huang, Q., Shi, B., et al. (2023). Nanocrystalline silicon-oxygen based tunneling recombination junctions in perovskite/silicon heterojunction tandem solar cells. EuroSun2004 *262*, 112539.

32. Zhu, L., Xu, Y., Zhang, P., Shi, J., Zhao, Y., Zhang, H., Wu, J., Luo, Y., Li, D., and Meng, Q. (2017). Investigation on the role of Lewis bases in the ripening process of perovskite films for highly efficient perovskite solar cells. J. Mater. Chem. A *5*, 20874–20881.

33. Wen, X., Cai, Q., Shen, G., Xu, X., Dong, P., Du, Y., Dong, H., and Mu, C. (2021). Enhanced crystallization of solution-processed perovskite using urea as an additive for large-grain MAPbI3perovskite solar cells. Nanotechnology *32*.

34. Han, L., Cong, S., Yang, H., Lou, Y., Wang, H., Huang, J., Zhu, J., Wu, Y., Chen, Q., Zhang, B., et al. (2018). Environmental-Friendly Urea Additive Induced Large Perovskite Grains for High Performance Inverted Solar Cells. Sol. RRL *2*, 1800054.

35. Chen, B., Baek, S.-W., Hou, Y., Aydin, E., de Bastiani, M., Scheffel, B., Proppe, A., Huang, Z., Wei, M., Wang, Y.-K., et al. (2020). Enhanced optical path and electron diffusion length enable high-efficiency perovskite tandems. Nat. Commun. *11*, 1257.

36. Cai, Q., Liang, C., Lin, Z., Zhang, W., Shen, G., Dong, H., Xu, X., Wang, H., Mu, C., and Xing, G. (2022). High-performance perovskite solar cells resulting from large perovskite grain size enabled by the urea additive. Sustainable Energy Fuels *6*, 2955–2961.

37. Zou, Q., Zheng, G., Yao, D., Wang, J., Tian, N., Mo, S., and Long, F. (2023). Effects of Lead Iodide Crystallization on Photovoltaic Performance of Perovskite Solar Cells by the Vapor-Solid Reaction Method. ACS Omega *8*, 12430–12438.

38. Rühle, S. (2016). Tabulated values of the Shockley–Queisser limit for single junction solar cells. Sol. Energy *130*, 139–147.

39. Farag, A., Fassl, P., Hu, H., Feeney, T., Quintilla, A., Ruiz-Preciado, M.A., Hempel, W., Bagrowski, D., Noack, P., Wattenberg, B., et al. (2023). Mitigation of Open-Circuit Voltage Losses in Perovskite Solar Cells Processed over Micrometer-Sized-Textured Si Substrates. Adv. Funct. Materials *33*, 2210758.

40. Fischer, O., Bui, A.D., Schindler, F., Macdonald, D., Glunz, S.W., Nguyen, H.T., and Schubert, M.C. (2023). Versatile Implied Open-Circuit Imaging Method and its Application in Monolithic Tandem Solar Cells. Progress in Photovoltaics, 1–14.

41. Choi, H., Choi, K., Choi, Y., Kim, T., Lim, S., and Park, T. (2020). A Review on Reducing Grain Boundaries and Morphological Improvement of Perovskite Solar Cells from Methodology and Material-Based Perspectives. Small Methods *4*, 1900569.

42. Hoefler, S.F., Trimmel, G., and Rath, T. (2017). Progress on lead-free metal halide perovskites for photovoltaic applications: a review. Monatsh. Chem. *148*, 795–826.

43. Gao, Q., Qi, J., Chen, K., Xia, M., Hu, Y., Mei, A., and Han, H. (2022). Halide Perovskite Crystallization Processes and Methods in Nanocrystals, Single Crystals, and Thin Films. Adv. Mater. *34*, e2200720.

44. Hu, H., Singh, M., Wan, X., Tang, J., Chu, C.-W., and Li, G. (2020). Nucleation and crystal growth control for scalable solution-processed organic–inorganic hybrid perovskite solar cells. J. Mater. Chem. A *8*, 1578–1603.

45. Liu, C., Cheng, Y.-B., and Ge, Z. (2020). Understanding of perovskite crystal growth and film formation in scalable deposition processes. Chem. Soc. Rev. *49*, 1653–1687.

46. Sánchez, S., Pfeifer, L., Vlachopoulos, N., and Hagfeldt, A. (2021). Rapid hybrid perovskite film crystallization from solution. Chem. Soc. Rev. *50*, 7108–7131.

47. Song, S., Yang, S.J., Choi, W., Lee, H., Sung, W., Park, C., and Cho, K. (2020). Molecular Engineering of Organic Spacer Cations for Efficient and Stable Formamidinium Perovskite Solar Cell. Advanced Energy Materials *10*, 2001759.

48. Lu, H., Liu, Y., Ahlawat, P., Mishra, A., Tress, W.R., Eickemeyer, F.T., Yang, Y., Fu, F., Wang, Z., Avalos, C.E., et al. (2020). Vapor-assisted deposition of highly efficient, stable black-phase FAPbI3 perovskite solar cells. Science *370*, eabb8985.

49. Park, J., Kim, J., Yun, H.-S., Paik, M.J., Noh, E., Mun, H.J., Kim, M.G., Shin, T.J., and Il Seok, S.I. (2023). Controlled growth of perovskite layers with volatile alkylammonium chlorides. Nature *616*, 724–730.

50. Chen, Z., Zhang, H., Yao, F., Tao, C., Fang, G., and Li, G. (2020). Room Temperature Formation of Semiconductor Grade α-FAPbI3 Films for Efficient Perovskite Solar Cells. Cell Rep. Phys. Sci. *1*, 100205.

51. Li, G., Zhang, T., Xu, F., and Zhao, Y. (2017). A facile deposition of large grain and phase pure α-FAPbI3 for perovskite solar cells via a flash crystallization. Mater. Today Energy *5*, 293–298.

52. Du, T., Macdonald, T.J., Yang, R.X., Li, M., Jiang, Z., Mohan, L., Xu, W., Su, Z., Gao, X., Whiteley, R., and Lin, C.T. (2022). Additive-Free, Low-Temperature Crystallization of Stable α-FAPbI3 Perovskite. Advanced Materials *34*, 2107850.

53. Zhao, Y., Tan, H., Yuan, H., Yang, Z., Fan, J.Z., Kim, J., Voznyy, O., Gong, X., Quan, L.N., Tan, C.S., et al. (2018). Perovskite seeding growth of formamidinium-lead-iodide-based perovskites for efficient and stable solar cells. Nat. Commun. *9*, 1607.

54. Xu, C., Zhang, Z., Zhang, S., Si, H., Ma, S., Fan, W., Xiong, Z., Liao, Q., Sattar, A., Kang, Z., and Zhang, Y. (2021). Manipulation of Perovskite Crystallization Kinetics via Lewis Base Additives. Adv. Funct. Materials *31*, 2009425.

55. Li, Z., Klein, T.R., Kim, D.H., Yang, M., Berry, J.J., van Hest, M.F.A.M., and Zhu, K. (2018). Scalable fabrication of perovskite solar cells. Nat. Rev. Mater. *3*, 1–20.

56. Cao, X., Li, C., Li, Y., Fang, F., Cui, X., Yao, Y., and Wei, J. (2016). Enhanced performance of perovskite solar cells by modulating the Lewis acid-base reaction. Nanoscale *8*, 19804–19810.

57. Levine, I., Al-Ashouri, A., Musiienko, A., Hempel, H., Magomedov, A., Drevilkauskaite, A., Getautis, V., Menzel, D., Hinrichs, K., Unold, T., et al. (2021). Charge transfer rates and electron trapping at buried interfaces of perovskite solar cells. Joule *5*, 2915–2933.

58. Iqbal, Z., Félix, R., Musiienko, A., Thiesbrummel, J., Köbler, H., Gutierrez-Partida, E., Gries, T.W., Hüsam, E., Saleh, A., Wilks, R.G., et al. (2024). Unveiling the Potential of Ambient Air Annealing for Highly Efficient Inorganic CsPbI3 Perovskite Solar Cells. J. Am. Chem. Soc. *146*, 4642–4651.

59. Gries, T.W., Regaldo, D., Koebler, H., Putri, T.N.H., Sannino, G.V., Partida, E.G., Felix, R., Huesam, E., Saleh, A., Wilks, R.G., et al. (2024). Enhanced Electron Extraction in Co-Doped TiO2 Quantified by Drift-Diffusion Simulation for Stable CsPbI3 Solar Cells. Preprint at arXiv.

60. Musiienko, A., Ceratti, D.R., Pipek, J., Brynza, M., Elhadidy, H., Belas, E., Betušiak, M.,

Delport, G., and Praus, P. (2021). Defects in Hybrid Perovskites: The Secret of Efficient Charge Transport. Adv. Funct Mater. *31*, 2104467.

61. Pradhan, R.R., Eswaran, M.K., Subbiah, A.S., Babayigit, A., de Wolf, S., and Schwingenschlögl, U. (2023). Elucidating the Role of Contact-Induced Gap States and Passivation Molecules at Perovskite/Metal Contacts. ACS Appl. Energy Mater. *6*, 4111–4118.

62. Li, X., Zhang, W., Guo, X., Lu, C., Wei, J., and Fang, J. (2022). Constructing heterojunctions by surface sulfidation for efficient inverted perovskite solar cells. Science *375*, 434–437.

63. Tischer, S., Börnhorst, M., Amsler, J., Schoch, G., and Deutschmann, O. (2019). Thermodynamics and reaction mechanism of urea decomposition. Phys. Chem. Chem. Phys. *21*, 16785–16797.

64. Shaaban, S.M., El-Sayed, B.A., Shabana, A.A., and Hassan, A.M. (1994). Temperature dependence of the electrical conductivity of urea and thiourea. Mater. Lett. *21*, 255–258.

65. Le Corre, V.M., Diekmann, J., Peña-Camargo, F., Thiesbrummel, J., Tokmoldin, N., Gutierrez-Partida, E., Peters, K.P., Perdigón-Toro, L., Futscher, M.H., Lang, F., et al. (2022). Quantification of Efficiency Losses Due to Mobile Ions in Perovskite Solar Cells via Fast Hysteresis Measurements. Sol. RRL *6*, 2100772.

66. Thiesbrummel, J., Le Corre, V.M., Peña-Camargo, F., Perdigón-Toro, L., Lang, F., Yang, F., Grischek, M., Gutierrez-Partida, E., Warby, J., Farrar, M.D., et al. (2021). Universal Current Losses in Perovskite Solar Cells Due to Mobile Ions. Adv. Energy Mater. *11*, 2101447.

67. Meusel, M., Adelhelm, R., Dimroth, F., Bett, A.W., and Warta, W. (2002). Spectral mismatch correction and spectrometric characterization of monolithic III-V multi-junction solar cells. Progress in PhotovoltaicsRes. Appl. *10*, 243–255.

68. Heydarian, M., Messmer, C., Bett, A.J., Heydarian, M., Chojniak, D., Kabaklı, Ö.Ş., Tutsch, L., Bivour, M., Siefer, G., Schubert, M.C., et al. (2023). Maximizing Current Density in Monolithic Perovskite Silicon Tandem Solar Cells. Sol. RRL *7*, 2200930.

69. Bett, A.J., Chojniak, D., Schachtner, M., Reichmuth, S.K., Kabaklı, Ö.Ş., Schulze, P.S.C., Fischer, O., Schindler, F., Hohl-Ebinger, J., Siefer, G., et al. (2023). Spectrometric Characterization of Monolithic Perovskite/Silicon Tandem Solar Cells. Sol. RRL *7*, 2200948.